Quaternary Science Reviews 251 (2021) 106718

Contents lists available at ScienceDirect

Quaternary Science Reviews

journal homepage: www.elsevier.com/locate/quascirev

Permafrost as a first order control on long-term rock-slope deformation in (Sub-)Arctic Norway

Paula Hilger [a, b, c, *], Reginald L. Hermanns [a, d], Justyna Czekirda [b], Kristin S. Myhra [b, c], John C. Gosse [e], Bernd Etzelmüller [b]

[a] Geohazards and Earth Observation, Geological Survey of Norway, Trondheim, N-7491, Norway
[b] Department of Geosciences, University of Oslo, Oslo, N-0316, Norway
[c] Department of Environmental Science, Western Norway University of Applied Sciences, Sogndal, N-6856, Norway
[d] Department of Geosciences and Petroleum, Norwegian University of Science and Technology, Trondheim, N-7491, Norway
[e] Department of Earth and Environmental Sciences, Dalhousie University, Halifax, B3H 4R2, Canada

ARTICLE INFO

Article history:
Received 2 July 2020
Received in revised form
13 November 2020
Accepted 16 November 2020
Available online xxx

Keywords:
Rockslides
^{10}Be and ^{36}Cl dating
Ground temperatures
Long-term reconstructions
Holocene
Norway

ABSTRACT

Assessing initiation of rock-slope deformation and paleo-slip rates of rockslides is important to understand the impact of climate variability - in particular permafrost changes - on rockslide activity. Norway, with 6–6.5% permafrost cover today, continues to experience spatial and temporal variations in permafrost. We assess the timing of deformation initiation and potential late Pleistocene and Holocene sliding rates for six active gradually deforming rockslides in Norway using terrestrial cosmogenic nuclide dating. We evaluate the timing and rates of deformation considering a possible climate control by modelling the permafrost evolution since deglaciation for three rockslide locations: Mannen, Revdalsfjellet and Gamanjunni 3. Deformation at these sites started during or at the end of the Holocene Thermal Maximum (HTM), between 8 and 4.5 ka when permafrost in those regions was mostly degraded. At two low elevation sites, Oppstadhornet and Skjeringahaugane in western Norway, where permafrost remained absent during the Holocene, deformation started shortly after deglaciation. The timings suggest that the presence of permafrost in Norwegian rock slopes had a stabilizing effect over several millennia after deglaciation. Vertical transects of exposure ages along outcropping sliding surfaces indicate that pre-historical sliding rates seem to have decreased throughout the Holocene at all analysed rock-slope instabilities. However, modern measured sliding rates at four sites indicate a moderate to strong acceleration, compared to previous deformation rates. Three of these sites are located above or at the lower limit of alpine permafrost, where recent permafrost degradation may enhance slope destabilisation. The implication is that slope failures may become more frequent during accelerated warming in the Arctic and Subarctic.

© 2020 The Author(s). Published by Elsevier Ltd. This is an open access article under the CC BY license (http://creativecommons.org/licenses/by/4.0/).

1. Introduction

In previously glaciated mountain ranges, rock-slope failure processes such as large gradually deforming rockslides and catastrophic rock avalanches contribute significantly to paraglacial landscape response and evolution (Ballantyne, 2002). In these regions, slope instabilities often pose a direct or indirect threat to the population and infrastructure in inhabited areas (e.g. Grimstad and Nesdal, 1991; Guzzetti, 2000; Hancox et al., 2005; Hermanns et al., 2012), where a comprehensive risk-assessment is essential. However, the prediction of rock avalanches remains difficult even in aseismic regions owing to the large number of non-linearly altering parameters affecting rock-slope stability (e.g. Eberhardt et al., 2004; Jaboyedoff and Derron, 2005, Gunzburger et al., 2005). It has been shown in Norway and the European Alps that there can be a close relation between long-term slope deformation and rock avalanches (e.g. Braathen et al., 2004; Ostermann and Sanders, 2017). This is supported by the theory of progressive failure, which was initially introduced for *'slope creep'* mechanics in soils (Terzaghi, 1950; Haefeli, 1953) and has been adapted for rock masses (e.g. Cruden, 1971; Eberhardt et al., 2004). It describes a non-linear '*creeping*' development of unstable bedrock slopes with

* Corresponding author. Department of Environmental Science, Western Norway University of Applied Sciences, Sogndal, N-6856, Norway.
E-mail address: paula.hilger@hvl.no (P. Hilger).

https://doi.org/10.1016/j.quascirev.2020.106718
0277-3791/© 2020 The Author(s). Published by Elsevier Ltd. This is an open access article under the CC BY license (http://creativecommons.org/licenses/by/4.0/).

potential for sudden acceleration initiating a catastrophic failure (Eberhardt et al., 2002; Petley et al., 2002, Crosta and Agliardi, 2003; Amitrano and Helmstetter, 2006; Lacroix and Amitrano, 2013; Roberts et al., 2019). Gradually deforming rockslides thus indicate the location of potential catastrophic rock avalanches and are therefore mapped systematically in Norway (Oppikofer et al., 2015; NGU, 2020a).

More than 583 slopes in Norway are characterised as unstable (Fig. 1), which means that open cracks, sliding surfaces or other morphological delimitations indicate post-glacial deformation of a rock mass (Oppikofer et al., 2015). Today, seven rockslides are monitored continuously by geodetic measurements, while the deformation of 90 localities is monitored episodically or periodically (Oppikofer et al., 2015; Blikra et al., 2016; NGU, 2020a). These seven rock-slope instabilities have been classified as high-risk sites (Hermanns et al., 2013a) owing to their high degree of deformation, recent activity, and potential impact on life and infrastructure (NGU, 2020a).

Assessing the current and future rockslide hazard requires that internal and external driving factors are identified and evaluated (Crozier and Glade, 2005; Hermanns et al., 2006). Besides structural pre-conditions, glacial debuttressing, seismicity, and rock fatigue - which have been linked to many rock avalanches shortly after deglaciation (Evans and Clague, 1994; McColl, 2012; Böhme et al., 2015b; Hermanns et al., 2017; Hilger et al., 2018) - a potentially significant parameter is weather and climate variation with respect to air temperature, precipitation and snow melt (e.g. Crozier, 2010; Moore et al., 2011; Blikra et al., 2012; Blikra and Christiansen, 2014). Precipitation influences the hydrostatic pressure conditions in steep slopes on day to millennial time scales (Hutchinson, 1988). Centennial to millennial changes in air temperature affect ground temperatures to great depths, and thus alter the subsurface ground thermal regime and permafrost in arctic and high-mountain environments. Cool and stable permafrost conditions, with temperatures below −2 °C may stabilise deep rockslides, while warm degrading permafrost decreases rock stability and effective shear strength (e.g. Gruber and Haeberli, 2007; Huggel et al., 2012; Krautblatter et al., 2013). Mechanical rock damage has been linked to the permafrost table and attributed to repeated cycles of seasonal ice segregation (e.g. Murton et al., 2006; Hales and Roering, 2007). Additional forces acting on permafrost-affected rock slopes are fluctuating thermal gradients and consequent tensional strains, volumetric expansion by freezing water in ice-blocked fractures, and hydrostatic pressure in fractures, which all induce fracturing and irreversible rock fatigue (Weber et al., 2017; Mamot et al., 2018). Knowledge of long-term thermal evolution of a rock slope therefore provides valuable insight into progressive rock deformation and related rockslides and rock avalanches. One approach to link late Pleistocene and Holocene climatic changes and related permafrost alterations to rock slope instability is to demonstrate a correlation between timing of initial deformation or changes in slip rates to climate events. This is possible with terrestrial cosmogenic nuclide (TCN) surface exposure dating, which is a useful tool to directly constrain both the failure timing of rock-avalanches (e.g. Ballantyne et al., 1998; Pánek 2015; Hermanns et al., 2017) and variation in sliding velocities of gradual gravitational bedrock deformation through time (Hermanns et al. 2012, 2013b; Zerathe et al., 2014). This approach is still undergoing development (Le Roux et al., 2009; Sanchez et al., 2010; Břežný et al., 2018), owing to the logistical, morphological and computational challenges of dating geometrically complex near-vertical sliding surfaces of actively deforming rockslides. In Norway a range of active but gradual motion on slip surfaces has been established with TCN dating, lending proof of the applicability and potential of this approach (Hermanns et al., 2012, 2013b; Böhme et al., 2019).

The objective of this study is to analyse the pre-historical development of six rockslides distributed over northern and western Norway to better assess the climatic conditions during deformation initiation, together with how climatic conditions may have contributed to a change in pre-historical slip rates. We address the interplay between the ground thermal regime, specifically mountain permafrost evolution, and the rockslide history. We present and integrate previously unpublished chronological data on three rockslides (Revdalsfjellet 1 and 2 in northern Norway and Mannen in western Norway), with data of the three previously published chronologies for the rockslides Gamanjunni-3 in northern Norway (Böhme et al., 2019), Skjeringahaugane (Hermanns et al., 2012) and Oppstadhornet (Hermanns et al., 2013b) in western Norway. We compare those chronological data in the context of long-term permafrost modelling based on different Holocene climate reconstructions. Additionally, we assess the thermal evolution at depth, for selected localities (Mannen, Revdalsfjellet and Gamanjunni 3), and compare the fluctuations with potential sliding patterns.

2. Setting and study sites

During most of the Last Glacial Maximum (LGM) (26.5-20 ka, Clark et al., 2009) the Norwegian mainland was completely covered by the Scandinavian Ice Sheet (e.g. Hughes et al., 2016; Stroeven et al., 2016). While large parts of the ice sheet were cold-based, warm-based outlet glaciers modified the pre-glacial landscape and shaped today's characteristic fjord and valley system along the coast (e.g. Kleman, 1994; Hall et al., 2013). During post-Younger Dryas deglaciation (after 11.5 ka), paraglacial landscape response initiated along the unbuttressed and oversteepened rock walls of the valleys and fjords, including supraglacial rock avalanches (Schleier et al., 2015). High post-glacial rock-fall and debris-flow activity resulted in extensive colluvial systems along the steep slopes (Blikra and Nemec, 1998). Additionally, a high density of on-shore and off-shore rock-avalanche and rockslide deposits, reaching beyond the talus, testify that these are the dominant processes modifying the conditionally unstable paraglacial landscape (e.g. Blikra et al., 2002; Böhme et al., 2015b; Hilger et al., 2018). Historical rock-avalanche events and many actively deforming unstable rock slopes demonstrate ongoing failure activity (Furseth, 1985; Grimstad and Nesdal, 1991), pre-failure deformation (NGU, 2020a), and associated risks.

In this study we reconstruct the sliding history of six rockslides: Oppstadhornet, Skjeringahaugane, Mannen, Revdalsfjellet 1, Revdalsfjellet 2 and Gamanjunni 3 (Fig. 2, Table 1). They were selected because of their risk-level and suitability for measuring paleo-slip rates. Today the climate at all sites is dominated by maritime humid conditions. The timing of deglaciation at the elevation of the instabilities ranges from 16 to 10 ka (Table 1), whereas final deglaciation of the valleys at Mannen, Revdalsfjellet and Gamanjunni was two to three millennia later. Today, the Mannen and Revdalsfjellet rockslides lie close to the regional lower limit of mountain permafrost in steep rock slopes (Magnin et al., 2019). Gamanjunni 3 reaches into continuous permafrost conditions, while the unstable slopes at Oppstadhornet and Skjeringahaugane lie several hundred metres below recent permafrost (Steiger et al., 2016; Gisnås et al., 2017; Magnin et al., 2019).

The most active rockslides today are Mannen and Gamanjunni 3, with measured deformation rates of ~ 2 cm a^{-1} and up to 6 cm a^{-1}, respectively. Both sites are classified as high-risk objects considering their high probability of failure (1/100 to 1/1000 years) combined with medium potential consequences (Dahle et al., 2008; Blikra et al., 2016; NGU 2020a), and are monitored continuously (NVE, 2017).

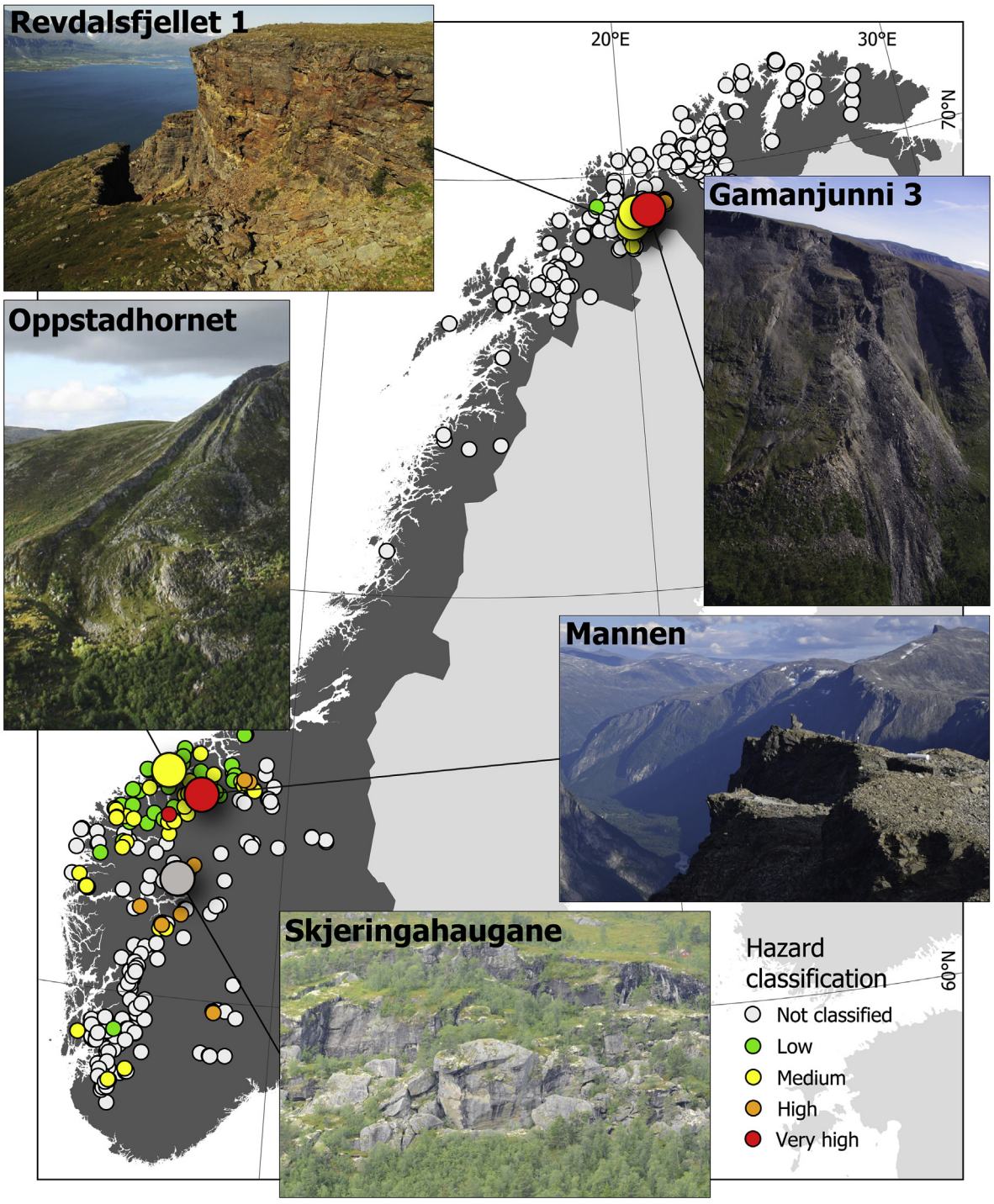

Fig. 1. Location of study sites and hazard classification of mapped unstable rock slopes in Norway (NGU, 2020a). The characteristic morphology with a sharp edge at the intersection of the plateau surface and slope indicates post-glacial deformation at most sites. Large circles are sites of the present study. Photos: H. Bunkholt (Revdalsfjellet and Gamanjunni), T. Oppikofer (Oppstadhornet) and R.L. Hermanns (Skjeringahaugane).

The Oppstadhornet rockslide exhibits 5–20 m foliation-parallel offset along a ca. 600 m long backscarp since initial deformation (Fig. 2a). Several less developed backscarps and open cracks indicate internal deformation of the unstable rock mass (Braathen et al., 2004). Because of the potentially extremely severe consequences related to displacement waves, the Oppstadhornet slope instability is classified as a high-risk object. However, the probability for potential failure remains low to medium because of its low deformation rates <0.5 cm a^{-1} (NGU, 2020a).

The Skjeringahaugane instability is divided into three segments (Figs. 2b and 3). Its total volume can only be estimated since the depths of the underlying sliding surfaces are not known. The upper ~10,000 m^2 segment is delimited by an open back fracture, which is covered with soil and vegetation, suggesting no recent deformation. This is different to the sparsely vegetated ~46,000 m^2 middle segment, which is broken into large blocks with 10–500 m^2

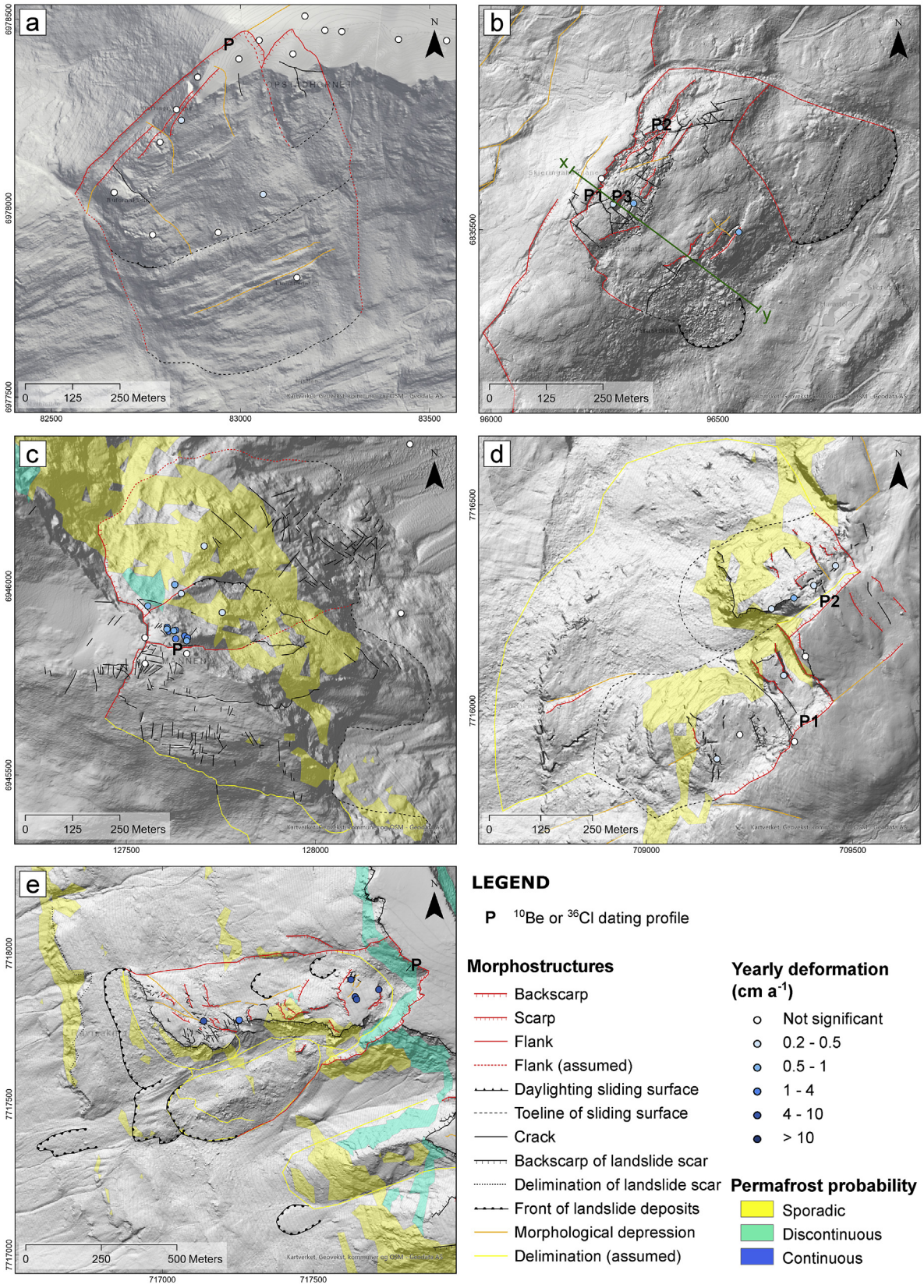

Fig. 2. Permafrost probability (data from Magnin et al., 2019) and morphostructures indicating deformation at the study sites Oppstadhornet (a), Skjeringahaugane (b), Mannen (c) Revdalsfjellet 1 and 2 (d) and Gamanjunni (e; NGU, 2020a). Azimut for artificial light source is 45° in a and 315° in b-e. Note the different scale in e.

Table 1
Most important characteristics of the studies rock-slope instabilities.

Name	Max. altitude	MAAT	MAP	Timing of deglaciation[a]	Estimated lower limit of discontinuous permafrost (>50% prob.)[b]	Dominating rock types[c]	Foliation[c]	Volume[d]	Hazard classification[d]	Risk classification[d]
	m a.s.l.	°C	mm	ka	m a.s.l.		dip	Mm^3		
Oppstadhornet	750	4–6	2000–3000	16–14	1400–1600	dioritic to granitic gneiss	steeply to moderately towards fjord	20	Low	High
Skjeringahaugane	750	2–4	1500–2000	11–10	1400–1500	phyllites andmica shists	15–20° towards fjord	80–200	Work in progress	Work in progress
Mannen	1295	0–2	2000–3000	14	1300–1400	dioritic to granitic gneiss	Near-vertical steeply dipping towards S	2–114	High	High
Revdalsfjellet 1	670	-2–0	1000–1500	14–12	700–1000	Garnet-mica shist, quartz-mica shist	sub-horizontal	0.8–7	Medium	Medium to high
Revdalsfjellet 2								<5	Medium	High
Gamanjunni 3	1200	-3–1	1000–1500	15–14	700–1000	Mica-shist	sub-horizontal	26	Very high	High

[a] References: Hughes et al. (2016), Stroeven et al. (2016).
[b] Reference: Magnin et al. (2019).
[c] References: Tveten et al. (1998), Roberts (2003), Bhasin and Kaynia (2004), Derron et al. (2005), Dahle et al. (2008), Hermanns et al. (2012), Saintot et al. (2012), Böhme et al. (2019).
[d] Reference: NGU (2020a).

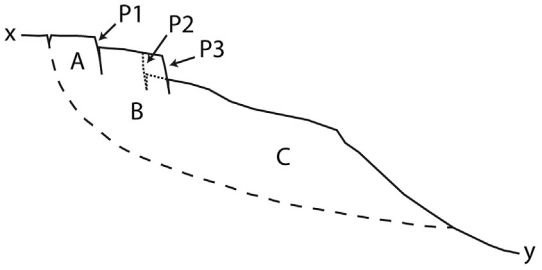

Fig. 3. Schematic profile x-y through the Skjeringahaugane instability (Fig. 2b). Sections A-C represent three segments of the instability with different deformation rates, also indicated in Hermanns et al. (2012). Transect P1, sampled for ^{10}Be exposure dating, represents the vertical displacement of segment B relative to the possibly stable section A, while the transects P2 and P3 represent displacement of segment C relative to B. Transect P2 represents this contact in the northeastern part of the instability (dotted line, cf. Fig. 2b), while P3 represents a subsection along the contact between B and C.

surface area, separated by deep open cracks (Photo in Fig. 1; Hermanns et al., 2011). The largest and lowest segment of the instability is characterised by large open cracks in an otherwise vegetated area. The lack of soil and vegetation in the cracks indicates recent deformation in both the middle and the lower part of the instability. The Skjeringahaugane instability is periodically monitored but not yet classified for hazard and risk. Recently measured rates of vertical deformation reach a maximum of 0.3 cm a^{-1} (NGU, 2020a). In this study, we present exposure ages along three vertical transects in the middle part of the Skjeringahaugane instability (Fig. 3). We have revised and re-calculated six surface samples previously published by Hermanns et al. (2012) and complemented these with four new measurements.

The deformation styles and recent activity at the four rock-slope instabilities Mannen, Revdalsfjellet 1 and 2 and Gamanjunni 3 are quite similar but different to the other two low-elevations sites. The most active parts of these rockslides are well delimited by near-vertical wedge shaped backscarps cutting through the sub-horizontal, or following the near-vertical foliation (Fig. 1). At Mannen, rock-slope failure deposits of six to nine distinguishable events at the bottom of the valley are evidence for a high Holocene rock-slope failure activity (Hilger et al., 2018). The Revdalsfjellet rockslides are two adjacent unstable rock masses along the same slope. Valley-parallel cracks in the slope indicate deformation almost down to the foot of the slope. Recent deformation rates of 0.2–0.3 cm a^{-1} at Revdalsfjellet 1 are connected to an estimated maximum volume of 800,000 m^3, while the whole instability comprises up to 7 Mm^3. At Revdalsfjellet 2 maximum deformation rates are 0.4–0.6 cm a^{-1} (NGU, 2020a). Potential consequences in case of a failure of any of the two instabilities are classified to be high. However, because of a low likelihood of failure of <1/5000 per year, the unstable rock mass Revdalsfjellet 1 is classified as an instability with medium to high risk. Unlike Revdalsfjellet 2, which is classified as a high-risk object, as a result of a medium failure probability of 1/1000 to 1/5000 years together with the severe potential consequences, such as displacement waves (Blikra et al., 2016). The Gamanjunni 3 rock-slope instability is located ca. 8 km east from Revdalsfjellet. The unstable rock mass at Gamanjunni is highly fractured, yet we observe a coherent sliding block with a relatively clear delimitation in the lower part of the slope (Fig. 2e). An up to 150 m long sliding surface separates the sliding block and its intact palaeo-surface from the original plateau surface (Böhme et al., 2016a, 2019).

3. Methods

3.1. ^{10}Be and ^{36}Cl exposure dating

TCN methods have been used to obtain exposure ages on landslide boulders to date *catastrophic* rock-slope failure events with measurement precisions of two centuries on mid-Holocene deposits in optimal sampling conditions and 2% coefficients of variation about mean boulder exposure ages (e.g. Hilger et al., 2018). To circumvent an unknown but possibly significant inherited concentration in rockslide boulders (Hilger et al., 2019) several studies have dated the failure scarps of *catastrophic* rock-slope failures by sampling cliff bedrock (e.g. Hermanns et al., 2004; Ivy-Ochs et al., 2009). Recently the TCN method has been used to date exposed sliding surfaces above *gradually* sliding blocks to monitor acceleration or deceleration in sliding rates over the Holocene (e.g. Le Roux et al., 2009; Hermanns et al., 2012; Zerathe et al., 2014; Březný et al., 2018; Böhme et al., 2019). The approach taken is similar to measurements of slip rates along exposed normal fault planes (e.g. Tikhomirov et al., 2014; Pousse-Beltran

et al., 2017; Tesson et al., 2019). In the fault slip rate approach, modelling efforts have focussed on computing the temporary shielding effect of transient colluvial wedges on the hanging wall. In the case of gradual gravitational rockslides, because the blocks often still exist, we can explicitly correct for ephemeral shielding by that moving block based on field measurements of the shield geometry.

Using chisel and hammer while on belay we sampled vertical transects over the sliding surfaces of three rock-slope instabilities in western Norway (Mannen, Møre og Romsdal) and northern Norway (Revdalsfjellet 1 + 2, Troms). Each transect consists of at least three samples for surface exposure dating. Additionally, we sampled the plateau surfaces above these transects with one sample each to correct for pre-sliding exposure history. This dataset of 14 samples was complemented by recalculated surface exposure ages for nine samples along four sliding surfaces at Skjeringahaugane, Vestlandet (Hermanns et al., 2011) and Oppstadhornet, Møre og Romsdal (Hermanns et al., 2013b). The existing dataset from Skjeringahaugane was additionally extended with four new sample measurements, to a total of 10 surface exposure ages. For comparison we also include data from a recently published transect from Gamanjunni 3, Kåfjord area (Böhme et al., 2019, Table 1), resulting in a total of 38 presented TCN measurements (Table 2). The fifteen new samples have been analysed for ^{10}Be in quartz, and three for ^{36}Cl in feldspar concentrates. All samples were processed as described by Hilger et al. (2018) and in

Table 2
Characteristics and location information for the samples (re-)analysed within this study. For completion, information about the recently published Gamanjunni samples are added.

Site	Sample name	Lat.	Long.	Elev.	Rock type	Sample thickness	Dip direction/dip	Total shielding	Sampling year	Previously published
		dd	*dd*	*m asl*		*cm*	*degree*	*unitless*		
Oppst.	Opp-1	62.7	6.83	696	gneiss	3		0.770	2003	Hermanns et al. (2013b)
	Opp-4	62.7	6.83	689	gneiss	3		0.769	2003	
	Opp-5	62.7	6.83	687	gneiss	3		0.768	2003	
Skjeringahaugane	Profile 1									
	SKJ-01	61.44	7.42	779	phyllite	4	115/72	0.704	2008	
	SKJ-02[b]	61.44	7.42	777	phyllite	3	110/58	0.670	2008	
	SKJ-03	61.44	7.42	774	phyllite	2	114/55	0.692	2008	
	Profile 2									
	SKJ-04	61.44	7.42	738	phyllite	4	122/65	0.699	2008	
	SKJ-05[b]	61.44	7.42	736	phyllite	4	109/86	0.654	2008	Hermanns et al. (2012)
	SKJ-06[b]	61.44	7.42	728	phyllite	4	096/68	0.686	2008	
	SKJ-08	61.44	7.42	725	phyllite	5	111/60	0.724	2008	
	Profile 3									
	SKJ-09	61.44	7.42	757	phyllite	5	130/39	0.883	2008	
	SKJ-10[b]	61.44	7.42	754	phyllite	3	116/34	0.782	2008	
	SKJ-12	61.44	7.42	746	phyllite	3	117/58	0.702	2008	
Mannen	MANN-00[a]	62.46	7.77	1289	quarzite	2	flat	0.996	2015	
	MAN-02	62.46	7.77	1285	felsic gneiss	3	017/89	0.511	2009	
	MAN-03	62.46	7.77	1281	felsic gneiss	2.5	002/53	0.565	2009	
	MAN-05	62.46	7.77	1274	felsic gneiss	5	020/65	0.524	2009	
Revdalsfjellet 1	RDF-01[a]	69.46	20.36	645	quarzite	2	230/10	0.998	2015	
	REV-01	69.46	20.36	644	gneiss	6	326/80	0.684	2009	
	REV-02	69.46	20.36	641	gneiss	5.5	322/62	0.666	2009	
	REV-04	69.46	20.36	635	gneiss	2.5	315/82	0.652	2009	
	REV-06	69.46	20.36	631	gneiss	2	320/51	0.623	2009	
Revdalsfjellet 2	RDF-03[a]	69.46	20.36	676	gneiss	3	flat	0.998	2015	
	REV-11	69.46	20.36	675	gneiss	5	298/53	0.750	2009	
	REV-13	69.46	20.36	668	gneiss	2.5	300/59	0.662	2009	
	REV-16	69.46	20.36	661	gneiss	3	310/59	0.662	2009	
	REV-17	69.46	20.36	657	gneiss	3.5	310/59	0.715	2009	
Gamanjunni 3	GAM-01[a]	69.48	20.58	1200	vein quartz	3	268/08	0.999	2011	
	GAM-02	69.48	20.58	1196	vein quartz	2	196/67	0.676	2011	
	GAM-03	69.48	20.58	1193	vein quartz	2	209/47	0.836	2011	
	GAM-05	69.48	20.58	1180	vein quartz	3	192/83	0.701	2011	
	GAM-07	69.48	20.58	1169	vein quartz	3		0.671	2011	
	GAM-09	69.48	20.58	1161	vein quartz	3	211/61	0.703	2011	Böhme et al. (2019)
	GAM-11	69.48	20.58	1154	vein quartz	3		0.850	2011	
	GAM-13	69.48	20.58	1147	vein quartz	1	208/67	0.850	2011	
	GAM-14	69.48	20.58	1144	vein quartz	3		0.850	2011	
	GAM-15	69.48	20.58	1138	vein quartz	1	220/67	0.735	2011	
	GAM-16	69.48	20.58	1131	vein quartz	3	193/76	0.604	2011	

[a] Sample from stable flat plateau surface above sampled sliding surface.
[b] Processed and analysed during this study.

the Supplementary Material, at the Cosmic Ray Isotope Sciences at Dalhousie University (CRISDal) lab, Halifax, Canada. Accelerator mass spectrometry (AMS) measurements for ^{10}Be were conducted at Lawrence Livermore National Lab, California, USA and for ^{36}Cl at PRIME Lab, Purdue University, USA.

Particular attention was required to compensate for the reduction of cosmic ray radiation to sampled surfaces caused by shielding on the near vertical cliffs with complex 3D geometries which included small overhangs. Our standard protocol is to compute correction factors for local topographic shielding for each sample site using high resolution (0.5–5 m) LiDAR data and the MATLAB shielding calculator for oddly shaped objects by Balco (2014). For the shielding calculation, we extracted individual areas of interest (AOI) for each site and created triangulated digital elevation models as 3D objects, representing the area around the sliding surface (Fig. 4a). Because of computing limitations, the AOI were limited to 60 × 60 to 150 × 150 m, depending on the resolution of the data. However, sensitivity tests with larger areas did not result in significantly different results. Within the 3D blocks of the AOI, the sample locations were placed at depths less than 1 cm (Fig. 4b), since the sample thickness is considered later in the calculation of the production rates. Subsequently the shielding was simulated with 10,000 iterations for each sample. Each iteration represents a simplified incoming cosmic ray trajectory, randomly selected from all potentially effective directions (Fig. 4c). The final value for the topographic shielding for each sample represents the cumulative average shielding factor generated over the 10,000 iterations (Fig. 4d). Uncertainty in the shielding correction was estimated by selecting points in the surface above and below the midpoint of the sample. On some occasions with irregular surfaces the uncertainty was about 7%, but most were below 5% but asymmetric about the shielding value for the midpoint.

Preliminary ^{10}Be ages were then calculated with version 3 of the online exposure age calculator formerly known as the CRONUS-Earth online exposure age calculator written by G. Balco, 2017 using the LSDn scaling scheme. The premise is that the TCN concentrations measured along the exposed steep sliding surfaces of the creeping slope instabilities should reflect the timing when the slide surface was first exposed. The ages should decrease with elevation down the sliding surface if the slip was gradual, or there would be sections exhibiting equivalent exposure ages if the instability failed over one or more episodic events. However, in the upper 10 m of the top of the cliffs, the gradually exposing steep sliding surfaces of creeping slope instabilities are influenced by inherited nuclide concentrations, owing to cosmogenic nuclide production below the surface before failure along the slip face. This requires consideration of not only spallogenic production of the nuclides (and thermal neutron capture for ^{36}Cl) but also TCN production by deeply penetrating muons. Rock-slope instabilities in Norway usually develop at the transition from relatively flat plateau surfaces to steep glacially-eroded rock slopes (Fig. 5a). At such plateau surfaces, the distribution of effective incoming cosmic radiation is close to $2\pi/360^{\circ}$, which it is for horizontal unshielded surfaces (Fig. 5 center). After deglaciation and before direct exposure by sliding, nuclide production at the sample locations are not zero (depending in part on the extent of glacial erosion and shielding over the past million years), but depending on their depth, exponentially smaller than at the plateau surface (shading in Fig. 5b). To correct for inheritance, samples were taken from the top surfaces close to the sampled transects at Mannen, Revdalsfjellet

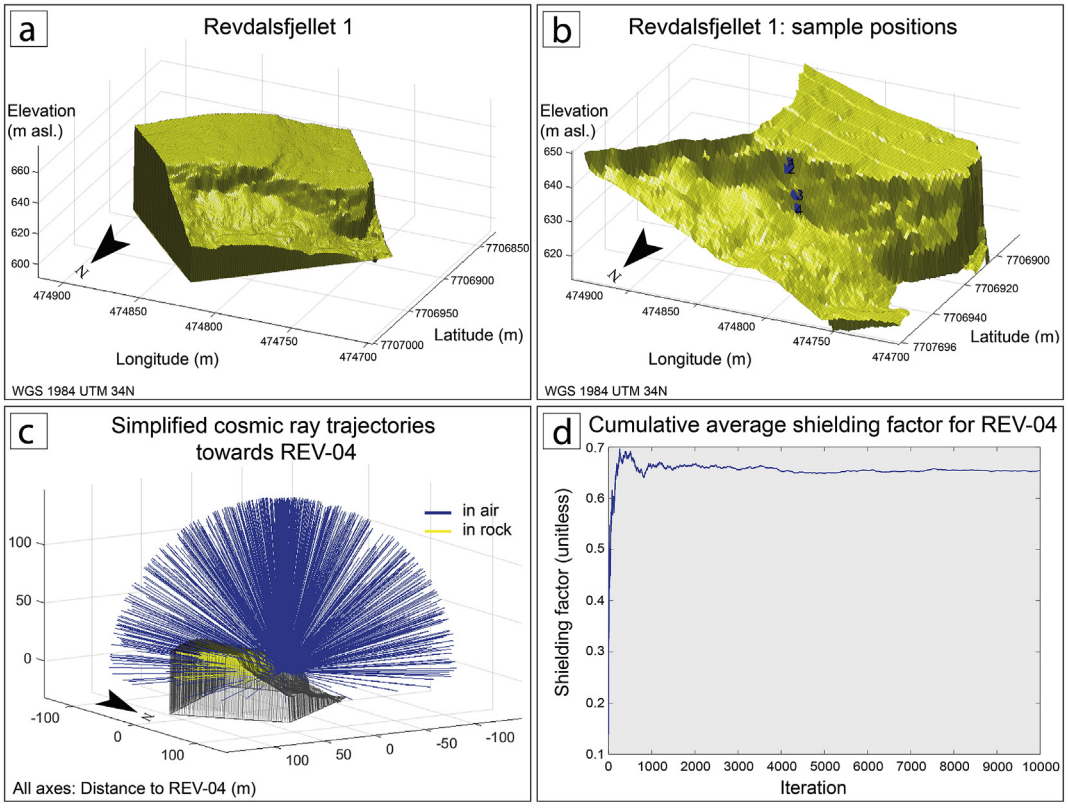

Fig. 4. Visualisation of the work-flow to derive the topographic shielding on a near-vertical cliff face with the computer code for estimating cosmic-ray shielding by oddly shaped objects (Balco, 2014): (a) 3D visualisation of the triangulated DEM, (b) sample locations, (c) simplified cosmic ray trajectories, each of which represents one iteration, (d) cumulative average shielding factor for 10,000 iterations.

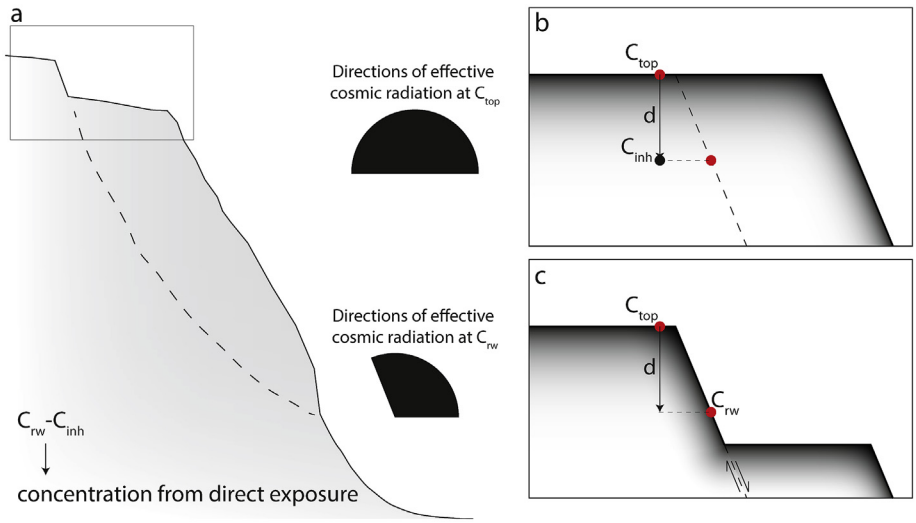

Fig. 5. Illustration of a rock-slope instability at the transition of a plateau surface into a steep rock wall (a), schematic of the position of a top sample (C_{top}) and a sample location along the (potential) sliding surface (b–c). Black/White scaling represents the exponential cosmogenic nuclide production at depth, resulting from the effective incoming cosmic radiation at the surfaces (center of figure).

and Gamanjunni 3. The ^{10}Be concentrations of these surfaces (C_{top}) indicate the timing of local deglaciation and potentially inherited concentrations from before the glaciation and allow for the reconstruction of the pre-failure ^{10}Be or ^{36}Cl concentrations (C_{inh}) at depth (approximately exponential). The pre-slide inheritance concentration will decrease predictably from the top of the cliff downward, and will be larger correction for recently exposed slide faces at the top of the cliffs.

Where samples on the plateau were not available, the pre-failure exposure time for the instabilities at Skjeringahaugane and Oppstadhornet were estimated considering regional deglaciation reconstructions (Hughes et al., 2016; Stroeven et al., 2016) and information about the erosional history of Sognefjorden (Andersen et al., 2018). This seems to be reliable as the Skjeringahaugane instability lies at the floor of a hanging valley into the former main ice stream and the Oppstadhornet mountain is the highest top of an island with smooth surfaces, both suggesting a strong glacial erosion during the last glacial cycle.

The previously calculated preliminary exposure ages are subsequently used to estimate the time between deglaciation and first exposure due to sliding at the sample location (C_{rw}) (Fig. 5c). Then, time-integrated sample-specific production rates were calculated iteratively, averaging the time and nuclide-dependent production rates for the corresponding period using the LSD scaling scheme (Lifton, 2016). Using the production rates for the three different pathways of ^{10}Be production (Table 3), the depth-dependent pre-failure ^{10}Be concentration (C_{inh}) at the sample location was approximated with the following equation (Gosse and Phillips, 2001):

$$C_{inh} = S\left[\frac{P_n}{\lambda}e^{\frac{-\rho d_i}{\Lambda n}}\left(1-e^{-\lambda\left(t_{top}-t_{rw}\right)}\right)+P_{\mu n}\Big/\ldots+P_{\mu f}\Big/\ldots\right] \quad (1)$$

where S represents the dimensionless shielding factor at the surface, $P_{n,\mu n,\mu f}$ (atoms g^{-1} a^{-1}) are the production rates for the three different pathways, spallation by fast nucleons (n), negative muon capture (μn) and fast muon reactions (μf), respectively, λ (a^{-1}) is the decay constant, ρ (g cm^{-3}) is the bulk density of the penetrated rock (in this study usually 2.6 g cm^{-3}), d_i (cm) is depth (vertically down), $\Lambda_{n,\mu n,\mu f}$ (g cm^{-2}) represent the attenuation lengths for each pathway, t_{top} (years) is the exposure age of the top surface and t_{rw} (years) is the approximated post-failure exposure time of each sample in the rock wall. The decay constant for ^{10}Be is 4.962×10^{-7} a^{-1}, based on the half-life of 1.387×10^{6} a (Chmeleff et al., 2010; Korschinek et al., 2010). The attenuation lengths 160 g cm^{-2}, 1500 g cm^{-2} and 5300 g cm^{-2} were used respectively for fast nucleons, negative muon capture and fast muon reactivations. The post-failure exposure time was derived subtracting the previously preliminary exposure ages from the estimated exposure age of the plateau surface. New and re-calculated ^{10}Be ages were derived using version 3 of the online exposure age calculator formerly known as the CRONUS-Earth online exposure age calculator written by G. Balco (2017) using the LSDn scaling scheme.

For the ^{36}Cl samples at the Mannen site, the CRONUScalc calculator (Marrero et al., 2016a) was used to derive the pre-failure ^{36}Cl concentration at depth for ^{36}Cl production rates based on Marrero et al. (2016b). The derived pre-failure concentrations (C_{inh}) were subsequently subtracted from the individually measured concentrations (C_{rw}). Note that usually only the uppermost one or two samples (within the upper 10 m of the top cliff edge) have any pre-slide concentrations to subtract. ^{36}Cl exposure ages were calculated with the CRONUScalc calculator using the SA scaling scheme in an iterative approach similar to ^{10}Be until a change in age was less than 1%.

For the derivation of the upper and lower limit of the potential timing of initial deformation, a linear approach was used, considering the 1σ internal uncertainties of the exposure ages along the sliding surfaces. For this, minimum sliding rates between the uppermost two samples of each transect are determined by calculating the time difference between the minimum age of the lower sample and the maximum age of the upper sample and subsequently dividing the distance along the sliding surface by this duration. Slope distances were measured in the field using a tape measure and have an asymmetric uncertainty attributed to overestimation caused by cliff roughness and incomplete stretching of the tape. Measurements from LiDAR data were normally within 5% 1σ. Maximum sliding rates are determined similarly, with the maximum age of the lower sample and the minimum age of the upper sample. The extrapolation of these sliding rates towards the top of the sliding surfaces localise the limits of the potential timing of initial deformation (Fig. 6). If the minimum timing of initial deformation was later than the minimum age of the uppermost

Table 3
Estimated exposure ages of four of the plateau surfaces and the derived production rates for the three different pathways based on the spallogenic ^{10}Be production rate of 3.98 atoms g^{-1} yr^{-1} at sea level and high geomagnetic latitude (SLHL).

Site	Oppstadhornet	Skjeringahaugane	Revdalsfjellet 1	Revdalsfjellet 2
Exposure age of plateau surface (ka)	15.5	11.0	11.2	10.3
Spallogenic/Neutrons (atoms g^{-1} yr^{-1})	8.13	8.72	7.76	7.98
Negative muons (atoms g^{-1} yr^{-1})	0.14	0.14	0.13	0.13
Fast muons (atoms g^{-1} yr^{-1})	0.05	0.05	0.05	0.05

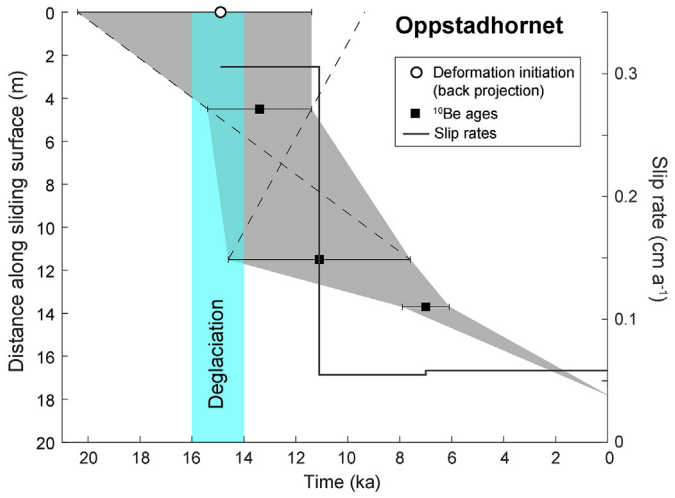

Fig. 6. ^{10}Be ages for Oppstadhornet (re-calculated from Hermanns et al., 2013b) with the envelope of possible displacement in grey and the slip rates according to the sample positions and ages. Dashed lines indicate the approach to approximate the upper and lower limit of the timing of initial deformation using the uncertainties of the two uppermost samples. This starting time is restricted by the minimum exposure age of the uppermost sample location. The approximated timing of initial deformation coincides with the period of local deglaciation after the LGM.

sample, the uncertainty was adjusted accordingly. For comparison, the same was done between the uppermost sample and the bottom of the sliding surface, using the average sliding rates over the whole distance.

3.2. Climate reconstruction

To assess a possible link between climate variation and the estimated sliding pattern of the rock-slope instabilities, we used combined long-term climate reconstructions for the Late Glacial and the Holocene, along with a simple glaciation model. These reconstructions were subsequently used as forcing for the two-dimensional permafrost model GryoGRID 2D (Myhra et al., 2017).

For thermal forcing of CryoGRID 2D we used the TraCE-21ka dataset, containing a simulation from 22 ka to 1990 CE (http://www.cgd.ucar.edu/ccr/TraCE/; Liu et al., 2009). The model is forced with transient greenhouse gas concentrations and orbitally-driven insolation changes, along with a transient scenario of meltwater forcing to the oceans from the retreating ice sheets. For our simulation a cell (3.75*3.75°, Yeager et al., 2006) for southern and northern Norway, respectively, was extracted and compared with the NGRIP ice core (NGRIP, 2004), where oxygen isotope relations were transferred to temperatures following a simple linear relationship provided in Johnsen et al. (1995). The TraCE-21ka data set performs poorly for the Holocene thermal maximum, so during 10 to 6 ka we corrected the data set with NGRIP ice core dataset. The re-constructed data were subsequently adjusted linearly to the climatic situation at the three sites, to the last normal period (1961-90), under the assumption of consistence between the general temperature patterns in Norway and Greenland (Lilleøren et al., 2012). We constructed air temperature forcing for each node along the slopes and at the flat plateau through a linear interpolation using a mean lapse rate of 0.63 °C 100 m^{-1} for Mannen and 0.45 °C 100 m^{-1} for Revdalsfjellet and Gamanjunni 3. For Gamanjunni, we modelled a profile stretching over the mountain ridge in SE-NW direction. Here, the south-western side of the rock wall temperatures are 1.5–2 °C warmer than the north-eastern side, following on-site rock wall temperature measurements in Magnin et al. (2019).

We used other datasets to visually compare the onset on rock slope movements and Late Glacial/Holocene climate variability. Lilleøren et al. (2012) incorporated five proxy datasets to derive the temperature deviation of mean July, mean January and mean annual air temperature (MAAT) from 10 ka to present in relation to the meteorological normal period 1961-90. These datasets were based on a speleothem analysis, Greenland ice core data and glacial mass balance derived from lake coring published in literature. The temperature anomalies are reconstructed separately for both northern and southern Norway. Mauri et al. (2015) reconstructed both temperature and precipitation anomalies for Europe over a period from 12 ka until the pre-industrial time (~1850 AD). That dataset is based on various pollen data from all over Europe, which has been calibrated and interpolated to produce 1 ° × 1 ° gridded maps. From this dataset, we extracted and analysed the available data over Norway to produce time series for northern and western Norway. For each grid cell, we initially extracted the time series of mean annual summer and winter temperatures, as well as mean and seasonal precipitation. Secondly, we grouped the single time series into reasonable regions, for which we finally combined the individual time series by averaging. To make the two reconstruction approaches with different reference periods comparable, the temperature data from Mauri et al. (2015) were corrected to represent the temperature anomalies according to the normal period 1961-90.

3.3. Thermal modelling

For evaluating the thermal regime at the study sites, we use CryoGrid 2D (Myhra et al., 2017), a process-based permafrost model in which the heat conduction equation with material and temperature dependent thermal parameters is solved by the finite element solver MILAMIN (Dabrowski et al., 2008) on a triangular mesh (Shewchuk, 1996). While the work scheme is described in more detail in Myhra (2016) and Myhra et al. (2017), we give a short overview over the main modelling steps:

The site-specific deglaciation dynamics are derived from a time-slice reconstruction of the Eurasian ice sheet (Hughes et al., 2016) combined with a simplified model of the glacier surface profile following Paterson (1994) and the assumption of perfect-plastic ice flow. The geometry of the model domain represents a 2D slice through the slope sections of interest. The triangular mesh is constructed with a depth dependent resolution and the simulations are run with yearly time steps. We assume identical bedrock conditions with granite-rich igneous rock as typically found in the Norwegian

basement and defined bedrock porosity 2% with water saturated conditions and set the bedrock thermal conductivity to 3.5 W °C^{-1} (e.g. Clauser and Huenges, 1995). The model is constructed with zero flux boundary conditions along vertical boundaries at elevations below the slope geometry and along the backside of the domain while a geothermal heat flux of 50 mW m^{-2} (Slagstad et al., 2009) is implemented along the bottom of the numerical domain (5000 m below sea level).

Along the slope and top of the domain, temperature forcing data are implemented through both glaciated (0 °C) and glacier-free periods by means of Dirichlet boundary conditions, where ground surface temperature, i.e. temperature below the snow and vegetation cover, is required as model forcing. We force glacier-free areas by the described temperature series from 20 ka to the beginning of the 20th century using annual time steps. During glacier-free periods, we assume snow accumulation on mountain plateaus and assume no snow accumulation along the steep slope. The snow is parameterised through a simple transfer factor, so-called *nF*-factor, reducing air freezing degree-days, and with this mimicking a certain snow cover. For the plateau at the top of Mannen, we use *nF*-factor of 0.3. For areas above ca. 640 m a.s.l. at the Revdalsfjellet site and the top plateau at Gamanjunni, we choose a *nF*-factor of 0.5. The differences of *nF* factors for the two sites are justified in the different average snow cover, which is almost double at Mannen (<2 m) compared to Gamanjunni/Revdalsfjellet (<1 m) in average. A *nF* factor of 0.5 corresponds to an annual mean height of snow of around 30 cm for a MAAT > −2 °C (Gisnås et al., 2013). To employ *nF*-factors for temperature forcing at yearly time steps, we compute mean monthly air temperature from SeNorge data for the normal period 1961–1990, add this seasonality to the yearly temperature, compute monthly ground surface temperature using *nF*-factors, and subsequently compute average annual ground surface temperature. To account for the slope aspect of the rock walls at Gamanjunni, air temperature at the south-western rock wall is adjusted with +1 °C, whereas air temperature at the north-eastern rock wall is adjusted with a factor of −1 °C.

The initial ground temperature conditions are obtained through a steady state simulation of the simplified rock wall geometry forced with surface temperature conditions of 0 °C, reflecting the ground temperature conditions in the late Weichselian when the Norwegian mainland was completely covered with glacial ice (Hughes et al., 2016). Under the assumption of temperate glaciers, this corresponds to initially unfrozen ground conditions and the modelled ground temperatures represent a minimum estimate of the permafrost extent, as the Scandinavian ice-sheet may have been mainly cold-based in high-mountain environments in central southern Norway (e.g. Kleman, 1994). To account for the uncertainty in the mentioned air temperature forcing data, four additional realizations of ground temperature modelling were run for each of the three sites, where the air temperature data were adjusted with factors of +0.5 °C, +1 °C, +1.5 °C and 2 °C. We note that despite having a reasonable control on snow cover which creates shielding from cosmic rays, we did not employ these constraints for the exposure chronology because we needed the concentration—not shielding-corrected age—of the plateau samples for the inheritance correction, and the steep slide surfaces dated did not likely retain sufficient snow cover.

4. Results

4.1. Geochronology

Oppstadhornet - The age recalculations for the Oppstadhornet rock-slope instability resulted in exposure ages of 13.4 ± 1.8, 11.1 ± 3.5 and 7.0 ± 0.8 ka from top to the bottom, respectively (Fig. 6; Table 4, age uncertainties are 1σ total error including internal random errors and external errors related to production rates). The results are respectively 900, 800 and 400 years younger than the previously published values, where no correction for vertical pre-failure exposure was conducted (Hermanns et al., 2013b). The resulting slip rates of 0.3, 0.05 and 0.06 cm a^{-1} agree within 0.02 cm a^{-1} with those calculated by Hermanns et al. (2013b). However, due to large 1σ uncertainties for the three individual samples, the significance of the sliding rates is limited. The large uncertainties are also represented in the time constraining of the initial deformation, which most likely started during or shortly after deglaciation between 16 and 15 ka. This is strongly supported by the morphology of the instability, with a sharp edge at the transition of the sliding surface to the mountain plateau.

Skjeringahaugane – Three vertical profiles along different sliding surfaces at Skjeringahaugane are represented by three to four TCN samples each. There is little evidence for active rockfall processes on the sampled surfaces, wherefore the results are considered representative for the exposure history of the rockslide. The three samples at profile 1 resulted in exposure ages of 7.7 ± 0.2, 4.9 ± 0.3 and 2.6 ± 0.1 ka, respectively (Table 4). These ages suggest rather slow, insignificantly increasing deformation rates of 0.08 cm a^{-1}, 0.10 cm a^{-1} and 0.11 cm a^{-1} throughout the Holocene. The recent average deformation rate of the moving block below this transect for the period 2008–2017 is 0.4 cm a^{-1}, suggesting a moderate acceleration. But it has to be noted that the recent measurements represent deformation in 3D directions. Mid-section B (Fig. 3) of the unstable rock slope at Skjeringahaugane likely became active at 11.2 ± 1.4 ka, thus during or shortly after local deglaciation (~11 ka; Table 5).

The samples of profile 2 resulted in exposure ages of 7.8 ± 0.3, 7.7 ± 0.6, 6.1 ± 0.4 and 2.6 ± 0.1 ka, respectively (Table 4). The oldest and youngest ages are similar and equal to the respective exposure ages of profile 1. However, the greater distance between the upper and lower samples results in a higher average deformation rate of 0.26 cm a^{-1} for the 5.2 ka. The uppermost two samples suggest a high vertical deformation of 2.19 cm a^{-1} during the first hundred years of deformation. However, due to the overlap of their age uncertainties, this average slip rate may not be representative. The 2.2 m displacement could have been instant or sliding could have been as moderate as 0.16 cm a^{-1}. The average sliding rate decreases to 0.46 cm a^{-1} at ca. 7.7 ka and further to 0.17 cm a^{-1} between 6.1 and 2.6 ka. Over the last 2.6 ka vertical deformation seems to be as low as 0.01 cm a^{-1} indicating a stabilisation along this sliding surface. This is in agreement with a measured deformation rate close to zero at this part of the instability in recent years. The estimated timing of initial deformation at profile 2 is 8.0 + 2.5–0.5 ka (Table 5).

The three samples at profile 3 resulted in exposure ages of 4.5 ± 0.5, 4.6 ± 0.3 and 1.3 ± 0.1 ka, respectively (Table 4). The strongly overlapping exposure ages of the uppermost two samples, again suggest an instant or very rapid vertical displacement of 1.7 m ca. 4.5 ka ago. Similarly, at this transect, decreasing average deformation rates during the late Holocene can be observed. Between 4.6 and 1.3 ka the average vertical slip rate decreased to 0.33 cm a^{-1}, and subsequently to 0.18 cm a^{-1} since 1.3 ka. The recent 3D deformation rate of the rock mass below this transect is 0.70 cm a^{-1}, relatively high compared to the calculated Holocene slip rates. However, the comparison of profile 3 and this measurement point must be treated with care, because where the samples have been taken the rock wall is unstable, with recent displacement rates of 0.40 cm a^{-1} into a similar direction. The relative difference of the vertical displacement along this rock wall is probably less than 0.30 cm a^{-1}, which is close to the average pre-historical slip rate

Table 4
Selected analytical data and results of the age calculation, including measured concentration of ^{36}Cl in feldspar separates or ^{10}Be in quartz, correction for pre-failure produced cosmogenic nuclides and the final age determinations and according slip rates between the respective sample and the next sample.

Site	Sample name	^{36}Cl*or ^{10}Be concentration	^{36}Cl*or ^{10}Be concentration corrected	^{36}Cl*or ^{10}Be concentration uncertainty	Apparent exposure age	Exposure age uncertainty int.(ext.)	Slip rate	Slip rate min.	Slip ratemax.
		10^3 atoms g^{-1}	*10^3 atoms g^{-1}*	*10^3 atoms g^{-1}*	*ka*	*ka*	*cm a^{-1}*	*cm a^{-1}*	*cm a^{-1}*
Oppst.	Opp-1	99.71	99.49	13.46	**13.4**	1.8 (2.0)	0.30	700	0.09
	Opp-4	81.61	81.40	25.54	**11.1**	3.5 (3.5)	0.05	220	0.03
	Opp-5	51.66	51.33	5.58	**7.0**	0.8 (0.9)	0.06	0.07	0.05
Skj. P1	SKJ-01	50.88	50.21	1.59	**7.7**	0.2 (0.5)	0.08	0.06	0.12
	SKJ-02	31.32	30.75	2.13	**4.9**	0.3 (0.5)	0.10	0.08	0.14
	SKJ-03	17.53	16.96	0.71	**2.6**	0.1 (0.2)	0.11	0.10	0.12
Skj. P2	SKJ-04	49.17	48.73	1.79	**7.8**	0.3 (0.5)	2.19	0.16	220
	SKJ-05	45.51	45.27	3.02	**7.7**	0.6 (0.7)	0.46	0.26	2.37
	SKJ-06	36.84	36.65	2.49	**6.1**	0.4 (0.5)	0.17	0.14	0.21
	SKJ-08	17.15	16.90	0.70	**2.6**	0.1 (0.2)	0.01	0.01	0.01
Skj. P3	SKJ-09	36.37	35.67	3.68	**4.5**	0.5 (0.5)	165	0.19	165
	SKJ-10	33.37	32.90	2.30	**4.6**	0.3 (0.4)	0.33	0.28	0.39
	SKJ-12	8.74	8.41	0.60	**1.3**	0.1 (0.1)	0.18	0.16	0.20
Mannen	MANN-00	151.37	top sample	5.00	**11.0**	0.3 (1.0)			
	MAN-02	23.51	23.15*	2.59*	**6.6**	1.1	0.10	0.07	0.25
	MAN-03	27.37	26.79*	8.67*	**3.0**	1.0	7.33	0.46	733
	MAN-05	28.15	27.85*	2.67*	**2.9**	0.5	0.16	0.13	0.19
Rev. 1	RDF-01	95.53	top sample	2.63	**11.1**	0.3 (0.7)			
	REV-01	29.44	24.31	1.21	**4.3**	0.2 (0.3)	0.27	0.13	159
	REV-02	21.52	20.91	0.70	**3.7**	0.1 (0.3)	601	1.09	601
	REV-04	21.02	21.10	1.28	**3.8**	0.2 (0.3)	0.19	0.15	0.25
	REV-06	10.43	9.58	0.60	**1.7**	0.1 (0.2)	0.17	0.15	0.19
Rev. 2	RDF-03	90.29	top sample	2.56	**10.3**	0.3 (0.7)			
	REV-11	49.99	47.12	1.97	**7.3**	0.3 (0.5)	0.50	0.29	1.62
	REV-13	35.35	34.71	1.27	**6.0**	0.2 (0.4)	0.22	0.18	0.26
	REV-16	14.71	14.27	0.86	**2.4**	0.1 (0.2)	0.24	0.19	0.31
	REV-17	7.85	7.15	0.43	**1.1**	0.1 (0.1)	0.14	0.13	0.15
Gamanj. 3	GAM-05	54.70	48.80	2.90	**5.3**	0.5 (0.6)	1920	2.13	1920
	GAM-09	51.80	51.40	2.10	**5.3**	0.4 (0.5)	1.44	1.00	2.56
	GAM-15	38.30	38.30	1.39	**3.7**	0.3 (0.4)	0.41	0.32	0.58
	GAM-16	17.30	17.30	0.80	**2.0**	0.2 (0.2)	1.90	1.77	2.06

(Table 4). The data suggest that deformation at this part of the unstable rock slope initiated more than 2 ka later than the deformation along P2.

This example of instability reveals that internal destabilisation and stress re-organisation may play an important role in the development of rock-slope instabilities in that strain can be

Table 5
Estimated initial deformation timing, average pre-historical sliding rates and modern measured sliding rates.

Rockslide	Elevation	Initial deformation (method 1)[a]	Initial deformation (method 2)[b]	Average pre-historical sliding rate	Measured sliding rates (NGU, 2020a)	Recent acceleration?[c]
	m asl.	*ka*	*ka*	*cm a^{-1}*	*cm a^{-1}*	
Oppstadhornet	700	**14.9** + 5.5–3.5	**18.0** ± 2.7	0.10	<0.5	o
Skjeringahaug. P1	782	**11.2** ± 1.4	**10.6** ± 0.7	0.09	0.4	+
Skjeringahaug. P2	742	**8.0** + 2.5–0.5	**9.5** ± 0.7	0.20	–	–
Skjeringahaug. P3	762	**4.6** + 2.0–0.3	**5.4** ± 0.6	0.33	<0.7	o
Mannen	1289	**8.0** ± 1.7	**8.3** ± 1.4	0.24	~2.0	++
Revdalsfjellet 1	645	**4.4** ± 0.4	**4.8** ± 0.3	0.34	0.2–0.3	o
Revdalsfjellet 2	676	**7.5** ± 0.7	**7.7** ± 0.5	0.26	0.4–0.6	+
Gamanjunni 3	1200	**5.3** + 1.4–0.4	**5.9** ± 0.6	2.35	5.4	++

[a] Approximated based on the apparent exposure ages and uncertainties of the two uppermost samples.
[b] Approximated based on the apparent exposure age of the uppermost sample and the average slip rate in relation to today.
[c] ++→significant, +→ moderate, o→ no change.

partitioned over different segments at different times. While activity along the main sliding surface between the rather stable section A and the unstable middle section B (Figs. 2b and 3) is constantly low, activity along the contact between sections B and C seems to be irregular along the contact, creating new sub-sections with high deformation rates, such as along P3.

Mannen - The three samples from the near vertical sliding surface at the Mannen rock-slope instability result in apparent exposure ages from the top to the bottom of 6.6 ± 1.1, 3.0 ± 1.0 and 2.9 ± 0.5 ka, respectively (Table 4). Considering these ages, the sliding rate was relatively low with 0.10 cm a^{-1} between 6.6 and 3 ka, followed by a strong acceleration to an average sliding rate of 7.33 cm a^{-1} during some hundred years and finally slowing down to 0.16 cm a^{-1} since 3 ka. (Table 4). Today the rock wall shows high rockfall activity in places. We therefore suggest a second scenario of paleo-slip rates considering that the middle sample MAN-03 may represent the surface of a post-exposure rockfall event.

In this scenario, the average slip rate between 6.6 and 2.9 ka was 0.3 cm a^{-1} before slowing down to 0.16 cm a^{-1}. The average sliding rate over the entire slope from the uppermost sample down to the modern bottom of the sliding surface is 0.24 cm a^{-1}. The modern measured sliding rate at the Mannen rock-slope instability is ~2 cm a^{-1} (NVE, 2017; NGU, 2020a). Compared to both scenarios of Holocene slip rates, the recent sliding rates are an order of magnitude higher and indicate a strong acceleration. Based on the back calculations presented earlier, the sliding surface at Mannen became active around 8.0 ± 1.7 ka (Method 1, Table 5).

Revdalsfjellet 1 - The four samples from the near vertical sliding surface at the Revdalsfjellet 1 rock-slope instability result in apparent exposure ages from the top to the bottom of 4.3 ± 0.2, 3.7 ± 0.1, 3.8 ± 0.2 and 1.7 ± 0.1 ka, respectively (Table 4). Considering these ages, sliding rates were relatively high with 0.27 cm a^{-1} between 4.3 and 3.7 ka, followed by an almost instant displacement of 6 m. The vertical displacement was then slowing down to 0.19 cm a^{-1} between 3.8 and 1.7 ka and finally to 0.17 cm a^{-1}. The two middle samples at Revdalsfjellet 1, which are non-differentiable within their age uncertainties, suggest a sudden displacement of 6 m without a consequent catastrophic failure. It is possible that the sliding surface has been affected by small-scale rock fall after being exposed by sliding and thus the exposure age of the upper location represents the surface of such a post-slide rock fall event. However, striations at the lower part of the sliding surface and a small volume of rock-fall debris indicate limited rock-fall activity (Fig. 7). An alternative sliding rate between REV-01 and REV-04, disregarding REV-02 would be 1.43 cm a^{-1}. The recently measured sliding rates for the Revdalsfjellet 1 rockslide lie between 0.2 and 0.3 cm a^{-1}. The estimated timing of initial deformation at this site is relatively young, with 4.4 ± 0.4 ka (Table 5).

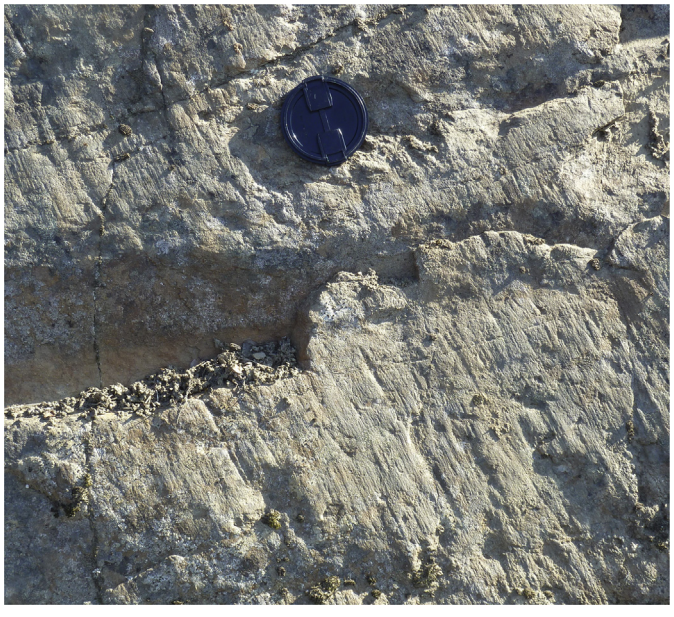

Fig. 7. Clearly visible striation in sliding direction on the lower section of the exposed sliding surface of Revdalsfjellet 1. Foto: H. Bunkholt (NGU).

Revdalsfjellet 2 - The four samples from the near vertical sliding surface at the Revdalsfjellet 2 rockslide result in apparent exposure ages from the top to the bottom of 7.3 ± 0.3, 6.0 ± 0.2, 2.4 ± 0.1 and 1.1 ± 0.1 ka, respectively (Table 4). The resulting sliding rates are 0.50 cm a^{-1} averaged over 1.3 ka, followed by 0.22 cm a^{-1} averaged over 3.6 ka, 0.24 cm a^{-1} over 1.3 and 0.14 cm a^{-1} during the last 1.1 ka. Recently, sporadic deformation measurements are carried out since 2009 (NGU, 2020a). They show a displacement of 0.4–0.6 cm a^{-1} and suggest a moderate acceleration compared to the sliding rates during the last 6.3 ka. The Revdalsfjellet 2 rockslide has most likely started to slide at 7.5 ± 0.7 ka (Table 5).

Gamanjunni 3 – The dating results of 11 samples from Gamanjunni 3 are more complex but show a general trend of 'younging' in the sliding direction along the sliding surface (Tables 4 and 5 based on results from Böhme et al., 2019). However, several samples are outliers in respect to the trend, generating age reversals in slide direction. Because of several potential sources for age underestimations along such a sliding surface compared to limited causes for age overestimations (Böhme et al., 2019), we focus on the four older surface exposure ages where we suspect no such discrepancy. The exposure ages for these older surfaces are 5.3 ± 0.5, 5.3 ± 0.4, 3.7 ± 0.3 and 2.0 ± 0.2 ka, respectively. Because the two uppermost samples have equivalent ages, initialisation of rock-slope deformation is estimated to be 5.3 ka. The two upper samples suggest a sudden initial deformation of several metres or very high deformation rates after sliding started. The average Holocene slip rate is 1.44 cm a^{-1} from 5.3 ka before slowing down to 0.41 cm a^{-1} and finally increasing again to 1.9 cm a^{-1} since 2 ka (Table 4). A large talus cone covering the lower 50 m of the sliding surface suggests a high and episodic rock-fall activity from portions of the slope above, and thus provides a potential explanation for low concentrations (and ages) for some of the other sample locations. However, the sliding rates indicate that deformation rates at Gamanjunni 3 have likely been continuously relatively high with a strong acceleration to the recently measured 5.4 cm a^{-1}.

4.2. Holocene climate variation and thermal modelling

The warmest period during the Holocene (Holocene thermal maximum, HTM) occurred near the end of the last glaciation, between 10 and 8 ka (e.g. Caseldine et al., 2006; Renssen et al., 2009). During this period, perihelion was during summer, resulting in warmer summers compared to today. MAAT were about 2 °C warmer than during the last normal period (1961–1990). Since the HTM, climate was gradually cooling, peaking with the Little Ice Age (LIA), which was around 1 °C (MAAT) colder than the last normal period. The modelled precipitation history is more complex. The TraCE-21 model indicates lower annual precipitation during HTM, except during summers, with an increase at around 6 ka. Ground temperature modelling of selected sites indicates that permafrost bodies have been developed during deglaciation (this study). The size and depth of these permafrost bodies depends on glacier dynamics during deglaciation and on elevation (Myhra, 2016; Czekirda, unpublished data).

Supplementary videos with the complete results of the thermal

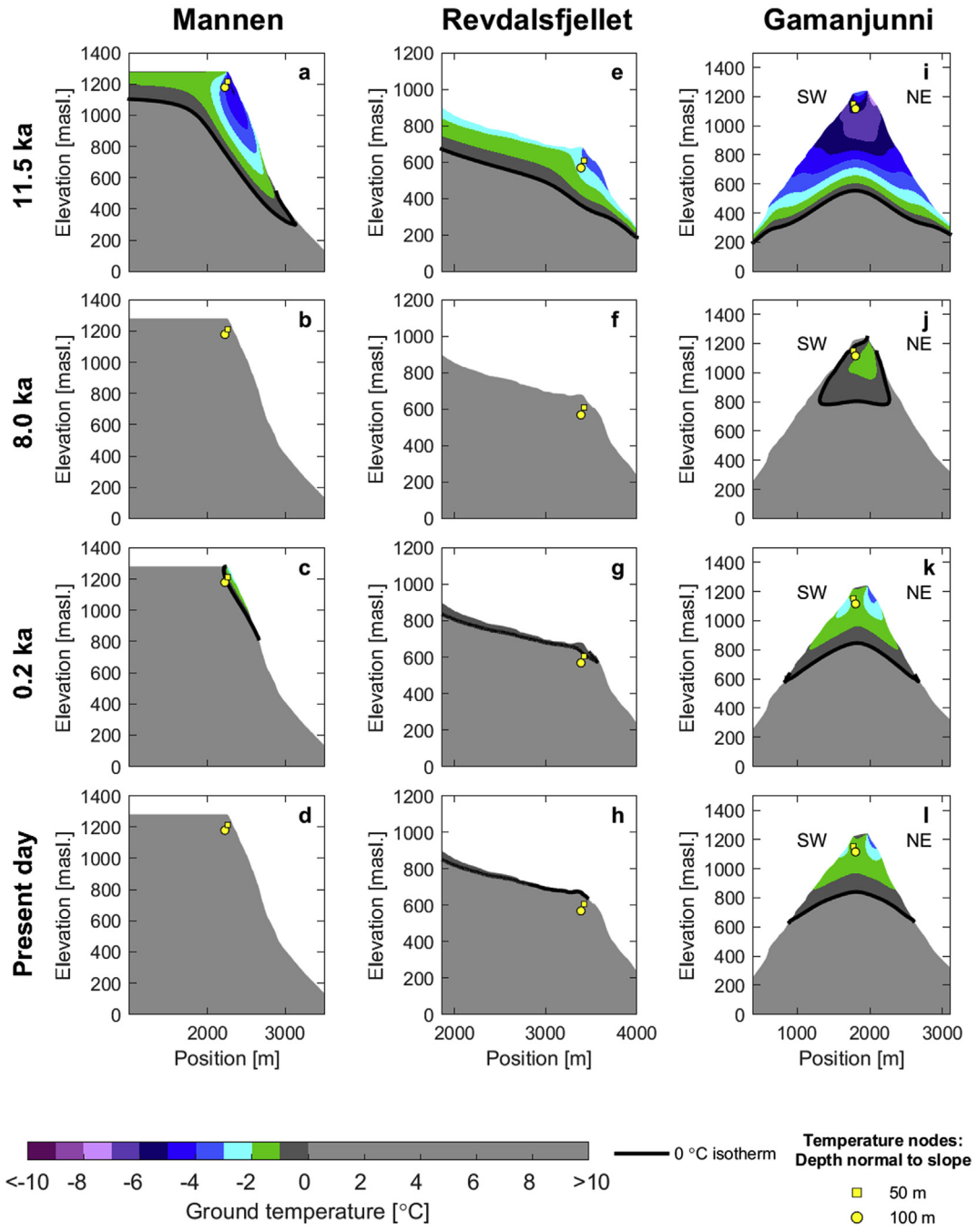

Fig. 8. Time slices of the long-term permafrost modelling results with CryoGRID 2D for Mannen, Revdalsfjellet and Gamanjunni for the realization with air temperature factor +0.5 °C. The temperature nodes indicate the approximate location of the upper most active parts of the rockslides. Their respective temperature curves from five realizations are plotted in Fig. 9. The complete results can be found as videos in the supplementary files.

modelling can be found at https://doi.org/10.1016/j.quascirev.2020.106718.

For Mannen, we assumed a start of deglaciation at 14 ka (Hughes et al., 2016) and that a 1300-yr YD glacial re-advance did not significantly affect permafrost conditions in the upper part of the slope. During and after deglaciation, cold permafrost remained deep into the slope at Mannen (Fig. 8a).

Rapid warming after the YD resulted in permafrost degradation and ground surface temperatures reaching positive temperatures up to 2 °C during the HTM (Figs. 8b and 9a). Between 5 and 3 ka, shallow ground (<50 m) in the northern slope might have reached negative temperatures during colder periods. According to the reconstruction, warm shallow permafrost re-established from c. 3 ka in the slope, culminating in the LIA, while the plateau remained above 0 °C (Fig. 8c). Today, Mannen is located at the lower boundary of regional mountain permafrost, with sporadic to discontinuous permafrost in the upper part of the slope (Fig. 2c; Magnin et al., 2019), which is not represented by the long-term model (Fig. 8d). Recent high-resolution modelling of the Mannen area indicates permafrost and deep seasonal frost in the area, which have degraded during the last decades (Kristensen et al., in review).

At Revdalsfjellet, the plateau above the rock-slope instabilities

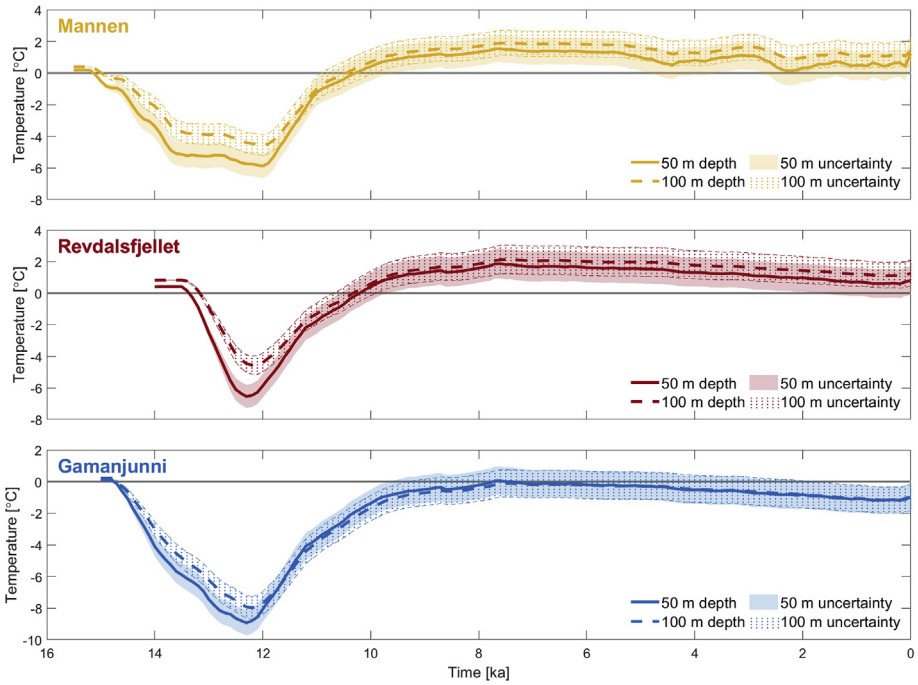

Fig. 9. Time series of ground temperatures at Mannen (a), Revdalsfjellet (b) and Gamanjunni 3 (c). The graphs represent the temperatures at 50 m and 100 m depth for each site (as indicated in Fig. 8), based on the long-term permafrost model. Results from five realizations are depicted, where the thickest lines correspond to mean ground temperature of all realizations, and uncertainty envelopes arise from the minimum and maximum ground temperatures of the remaining realizations.

was first deglaciated between 13 and 14 ka, with subsequent frost penetration into the slope (Fig. 8e). Relatively fast permafrost degradation initiated after the YD cold period, where a transition to warm permafrost conditions was modelled 11-10 ka. Modelled ground temperatures at 10 ka were 0 °C followed by a long period throughout the HTM with mostly positive temperatures (Figs. 8f and 9b). Since 2 ka, surface-near ground temperatures (<50 m) fluctuated around 0 °C again with increasing duration and depth of frozen ground conditions. Today, ground temperatures at the upper parts of the Revdalsfjellet instabilities still fluctuate around 0 °C (Fig. 8h), according to the mapping of steep permafrost slopes (Fig. 2d; Magnin et al., 2019) and the observations at the Nordnes rock-slope instability, a few kilometres north of Revdalsfjellet (Blikra and Christiansen, 2014).

At Gamanjunni a SW-NE transect through the entire ridge between two valleys was modelled. The thinning of the glacial ice from about 15 ka is directly followed by deep and cold permafrost conditions within the rock (Figs. 8i and 9c). The permafrost geometry is asymmetric as we here assume different temperature forcing for the south and north side, respectively, due to topography and modulated insulation effects (Magnin et al., 2019). After the YD, the permafrost degraded rapidly along the slopes, but negative ground temperatures could persist at depth until c. 8.5 ka according to the modelling, especially on the northern side. During the HTM, permafrost was probably degraded close to the surface, however, permafrost at depth may have still existed (Fig. 8j). The south-western slope seemed to remain at and above 0 °C until c. 2 ka (Fig. 9c). Since then rather warm permafrost has probably been in the mountain ridge, reaching considerable depths according to the modelling, especially during the LIA (Fig. 8k). For today, the long-term model still suggests the presence of warm permafrost in the mountain (Fig. 8l), which is in accordance with Magnin et al. (2019) and the regional modelling by Gisnås et al. (2017).

5. Discussion

5.1. Surface exposure dating along sliding surfaces

The number of studies presenting sliding surfaces of active rockslides successfully dated with cosmogenic nuclides remains limited. But our results and previous studies (e.g. Le Roux et al., 2009; Hermanns et al., 2012; Zerathe et al., 2014; Březný et al., 2018; Böhme et al., 2019) suggest that this is due to logistical and morphological challenges, rather than a lack of reliability of the method. The following observations suggest the gradual slip rate approach may be useful:

- The transects along the sliding surfaces of the rock-slope instabilities at Oppstadhornet, Skjeringahaugane, Mannen and Revdalsfjellet consist of three to four ^{10}Be or ^{36}Cl ages. Within one sigma uncertainty, they all show a logical chronological order decreasing with elevation.
- The geometry of the instabilities also indicate that the sliding surfaces have been exposed gradually from the top to the bottom.
- The sliding rock masses are represented by fractured blocks that are vertically displaced but still show the original surface in most cases. These rockslide blocks fit into their original position, allowing for optimal adjustment for shielding corrections and evidence for the gradual, non-catastrophic gravitational deformation implied by the ages.
- Reproducibility of the exposure age method is demonstrated by equivalent ages on adjacent surfaces and by the fact that several samples (REV-16, SKJ-02, -05, −06 and SKJ-10) were processed completely independently from the others and analysed by AMS at different times (sometimes different years), yet their result fit well into the chronology of the previously analysed samples of the same transect within 1σ uncertainty (Table 4).

These observations suggest that our field interpretation of limited rock fall activity from the sliding surface after being exposed by the rockslide is true in most cases. However, the effects of small-scale rock fall may result in underestimations of the apparent exposure age of a surface. While the presence of polish or vertically oriented striations, and absence of weathering, lichen cover, or patination of bedrock surfaces have been useful to guide sampling locations on a sliding surface, in a few instances we may have sampled surfaces with relatively recent small-scale falls. Furthermore, the build-up of a 50 m high talus cone covers the foot of the 140 m long sliding surface of Gamanjunni 3, evidencing small-scale periodic rock-fall activity along the slope (Böhme et al., 2019) and causing short-term shielding of the bedrock surface. The development of such a talus cone can only be estimated by comparing the age of the sliding surfaces with an average slip rate. In the case of Gamanjunni 3, the build-up of this cone may have led to an age offset of up to 2 ka.

5.2. Sliding patterns

Modelling approaches have hitherto dominated studies concerning the development of slow-moving rockslides over thousands of years (e.g. Welkner et al., 2010; Gischig et al., 2016; Agliardi et al., 2020; Donati et al., 2020). We attempted to fill the gap of measurements that document these phenomena. The average sliding rates between the exposure dated surfaces of this study result in similar sliding patterns for all transects, with high displacement rates after initialisation, followed by rather constant or decreasing displacement rates. However, with the number of samples available it is not possible to state where and when the transitions between different deformation rates occurred, or if there were variations of sliding rates in time that cannot be resolved due to the low sampling frequency. The higher number of samples at the Gamanjunni 3 rockslide result in a more complex pattern. Yet the sliding pattern generally shows a similar trend of higher displacement rates in the beginning and lower displacement rates during the last millennia (Böhme et al., 2019). These sliding patterns are in contrast to varying observed sliding patterns from the French Alps where in one case an acceleration phase between 2.3 and 1 ka initiates higher displacement rates (Sechilienne rockslide; Le Roux et al., 2009), or only continuous deformation rates of <0.04 cm a^{-1} since $\sim$3 ka were measured (Cair landslide; Zerathe et al., 2014).

Crosta and Agliardi (2003) and Xue et al. (2014) discuss the potential forecast of sudden rock avalanches based on the 'slope creep' behaviour of long-term slope deformations. The slope-creep model suggests an idealised deformation behaviour in three stages characterised by different ratios of shear force and shear resistance (Cornelius and Scott, 1993):

1. The primary phase is dominated by strongly increasing strain and development of fractures (Lacroix and Amitrano, 2013).
2. The secondary phase is characterised by a constant strain rate.
3. The tertiary phase initialises sudden failure by increasing strain and damage development resulting in accelerated deformation (Crosta and Agliardi, 2003; see also Petley et al., 2002; Stead and Eberhard, 2013; Roberts et al., 2019).

Our data generally supports this model, considering that initially high strain rates resulted in high sliding rates changing subsequently to relatively constant sliding rates. However, the development of unstable rock slopes in natural materials is not only dependent on slope geometry and internal factors, but it is also affected by several external parameters, that either decrease the shear resistance or increase driving forces. Gradual and sudden changes of external factors, such as climate or tectonic activity can hence modify the theoretical model and lead to a temporal increase or decrease of displacement rates.

5.3. Factors influencing the timing of initial deformation

There are internal and exogenic factors that control the timing of initial deformation at unstable rock slopes. A first-order internal control is the structural form of discrete discontinuities that can develop into failure surfaces (e.g. Eisbacher and Clague, 1984; Hermanns and Strecker, 1999; Brideau et al., 2009). This is especially true for the crystalline bedrock in Norway (e.g. Saintot et al., 2012; Böhme et al., 2013; Booth et al., 2015). Structural preconditioning has been reported for our study sites Oppstadhornet and Gammanjunni 3 (Bhasin and Kaynia, 2004; Böhme et al., 2016b). Also at Skjeringerhaugane mapping indicates that the highly fractured slope is related to pre-existing structures connected to shear and contact zones between the dominating phyllites within the instability, granitic gneiss in the lower part and meta-arkose above the instability (NGU, 2020b). The Gamanjunni and Revdalsfjellet rockslides are wedge failures, constrained by two steeply dipping joints and the shallow, out of the slope dipping, foliation.

Superimposed on that are external driving factors that vary in time such as (i) post-glacial isostatic uplift and potential related seismic activity, (ii) glacial unloading and debuttressing, and (iii) climatic factors such as ground thermal regime including permafrost degradation.

5.3.1. Post-glacial isostatic uplift and potential related seismic activity

Numerous observations document seismicity is a direct cause for rock-slope failure (e.g. Pareek et al., 2010). It can be argued that seismicity related to glacial isostasy (Lund and Näslund, 2009) may have added to destabilising rock slopes in Scandinavia. This effect would have been most significant during and shortly after deglaciation, when the isostatic rebound was most rapid (Ballantyne et al., 2014; Bellwald et al., 2019). A combination of inherited geological structures, deglaciation and long-term shallow seismicity have been discussed to substantially contribute to activating deep-seated rockslides in the Alps (Agliardi et al., 2019; Baroň et al., 2019). Potential shallow seismic activity may therefore be an additional exogenic factor for the Late Pleistocene and Early Holocene deformation at Oppstadhornet and Skjeringahaugane (Figs. 6 and 10). However, paleoseismological evidence for rock-slope failure is absent in Norway, despite trenching activity in the areas where our instabilities are located (Schleier et al., 2016). We cautiously propose that while seismicity is relevant for *catastrophic* rock-slope failures, the observed gradual sliding deformation is more likely attributable to climatic forcing.

5.3.2. Glacial unloading and debuttressing

At Oppstadhornet and the upper section of Skjeringahaugane, initial deformation directly followed local deglaciation at 16-14 and 11-10 ka, respectively (Figs. 6 and 10). The preserved sharp edge between the sliding surface and the mountain plateau at both sites minimises the likelihood of a pre-glacial onset. However, we do not preclude the potential effect of long-term rock fatigue due to repeated glacial cycles that might have resulted in instabilities prior to deglaciation and being reactivated shortly after deglaciation (Jia et al., 2015; Grämiger et al., 2017). Numerical modelling supports the destabilising effect of glacial unloading on rock slopes (Brückl, 2001), especially where pre-existing rock damage exists

(Grämiger et al., 2017).

5.3.3. Ground thermal regime including permafrost degradation

In previous studies regarding large deep-seated rockslides possible climatic and thermal effects are often mentioned, but discussed only briefly owing to limited control over pre-historical precipitation and ground thermal regime (e.g. Bigot-Cormier et al., 2005, Březný et al., 2018, Hilger et al., 2018). One critical factor for slope stability is the presence and warming of ice-filled rock joints (Krautblatter et al., 2013). Depending on the overburden, ground temperatures close to 0 °C can reduce the shear resistance along ice-filled fractures by more than 60% compared to cold permafrost conditions (Mamot et al., 2018). The ground thermal regime is a factor which has been much discussed as driver for recent rockfall and rock-avalanche activity (e.g. Gruber and Haeberli, 2007; Ravanel and Deline, 2011; Krautblatter et al., 2013), but rarely for creeping rock masses. During the last 20 years, evidence for the activation of large rock-slope instabilities due to permafrost degradation has been documented in the Alps, e.g. Keuschnig et al. (2015) (Austrian Alps); Lebrouc et al. (2013) (French Alps); Mamot et al. (2018) (Zugspitze, Germany); Weber et al. (2017) (Swiss Alps). Based on thermal numerical modelling at the Séchilienne Landslide in the French Alps it is suggested that cold permafrost has stabilized the slope for 3 to 4 ka after local deglaciation (Lebrouc et al., 2013). The authors argued that the permafrost body likely has amplified weaknesses caused by rock fatigue and the depth of rock fracturing due to debuttressing, but also that its stabilizing presence is one of the main reasons for delays of 6 ka or more before rockslide activation. Similarly long time lags have been observed in the Alps (e.g. Le Roux et al., 2009; McColl, 2012) in the western Carpathians (Pánek et al., 2017) and in the Himalaya (Dortch et al., 2009), indicating the influence of external driving factors.

The rockslides Mannen, Revdalsfjellet 2 and Gamanjunni 3 generally show a similar development, with a time lag at a millennial scale between deglaciation and the onset of deformation. At Mannen and Revdalsfjellet 2, the estimated timing of initial deformation coincides with the first peak of the HTM around 8 ka (Table 5, Figs. 10 and 11). Our thermal modelling of these sites indicates that the slopes have been affected by deep permafrost penetration during and after deglaciation; however, permafrost degraded substantially during the following millennia. Our model indicates that at Mannen and Revdalsfjellet ground temperatures at 50 and 100 m depth increased to >0 °C before 10 ka and reached a maximum between 8 and 7.5 ka, when slope deformation started (Fig. 9a and b). In comparison, deformation at Gamanjunni started ~3 ka later, near the end of the HTM (4.5 ka). Modelled ground temperatures at 50 and 100 m depth at Gamanjunni remained negative until ~8 ka and <1 °C throughout the HTM. The mountain could therefore have been sensitive to the short cooling event at 8.2 ka and remained affected by permafrost conditions throughout the HTM due to internal transient conditions (ice content in cracks etc.) and thermally controlled slower permafrost degradation. Significant permafrost warming and degradation is thus likely a destabilising factor for initial deformation at Norwegian unstable rock slopes, with the lower latitude rockslide Mannen and the low altitude rockslide Revdalsfjellet 2 reacting sooner than the high latitude and high elevation site Gamanjunni 3.

5.4. Factors influencing recent acceleration of slope deformation

At four study sites we observe moderately or significantly increased modern slip rates compared to Holocene deformation (Figs. 10 and 11; Table 5). This might be related to atmospheric warming after the Little Ice Age (LIA), which resulted in increased ground temperatures. This may specifically be true for the three rockslides Mannen, Revdalsfjellet 2 and Gamanjunni 3, where we

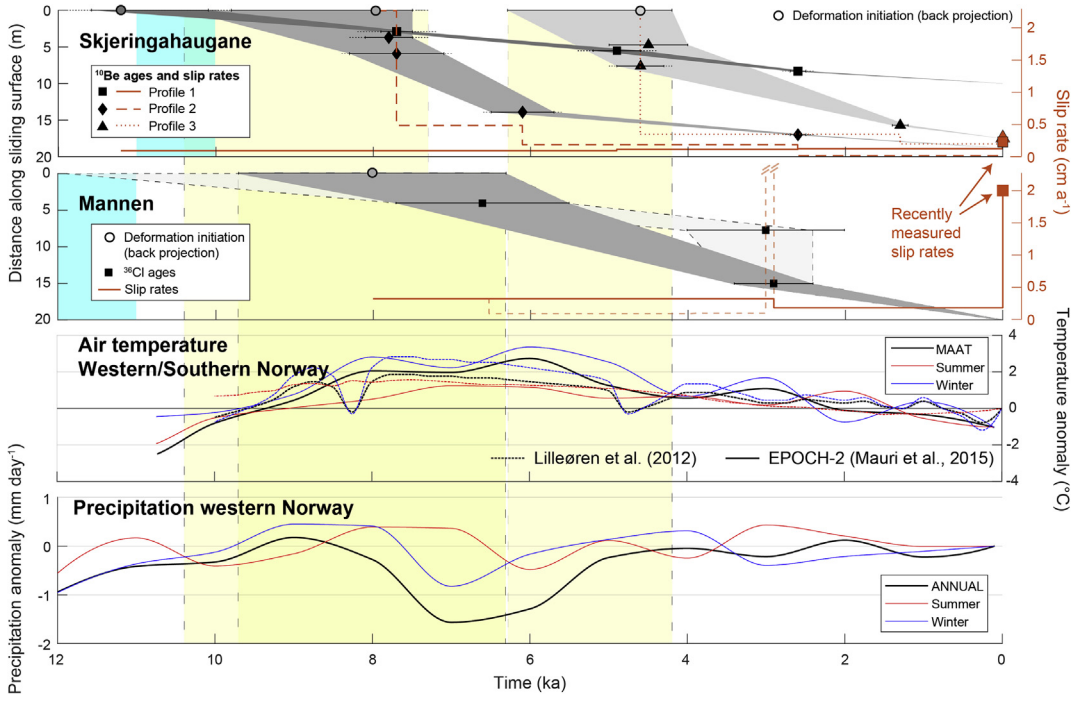

Fig. 10. Results of ^{10}Be and ^{36}Cl dating respectively along the sliding surfaces at the rock-slope instabilities Skjeringahaugane and Mannen above reconstructed series of temperature anomalies and precipitation changes. Internal and external uncertainties are plotted as horizontal continous and dotted lines, respectively. Note that summer and winter anomalies from Lilleøren et al. (2012) represent data from July and January, respectively, whereas Mauri et al. (2015) combine June, July and August and December, January and February, to represent the seasons.

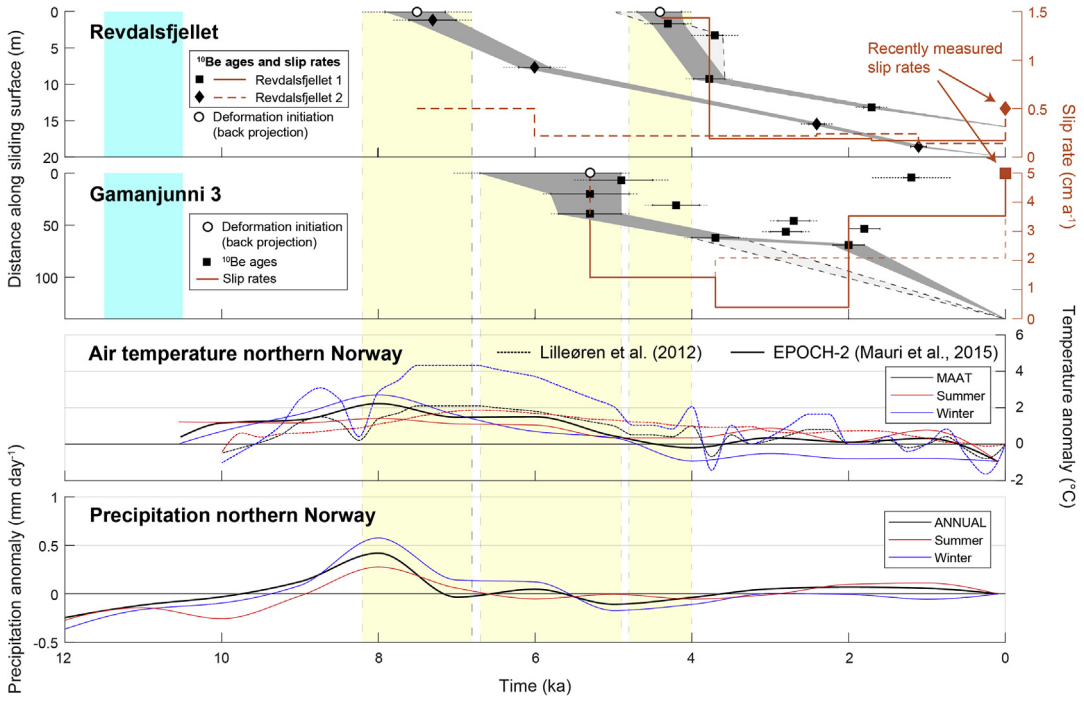

Fig. 11. Results of ^{10}Be dating along the sliding surfaces at the rock-slope instabilities Revdalsfjellet and Gamanjunni 3 (Böhme et al., 2019) above reconstructed series of temperature anomalies and precipitation changes. Internal and external uncertainties are plotted as horizontal solid and dotted lines, respectively.

here hypothesise that initial deformation was connected to climatic factors including permafrost degradation. The upper parts of all three sites are today located close to or above the estimated lower limit of mountain permafrost (Table 1; Magnin et al., 2019). Detailed research and monitoring at the active rock-slope instability at Nordnesfjellet, which is located in the same setting about 7 km north of Revdalsfjellet, revealed large permanently ice-filled fractures (Blikra and Christiansen, 2014). The locally very variable thermal regime seems to affect the modern slope stability, which reacts seasonally, with increasing activity during the summer and stable conditions during cold winter months. Therefore, recent deformation at the Revdalsfjellet rockslides may also be affected by local ice-rich permafrost in open fractures.

In addition to permafrost degradation, recently increasing precipitation rates and intensities (Dyrrdal et al., 2012) may be a factor for augmented slope destabilisation in Norway. Several studies support the hypothesis that both periodic and long-term displacement of deep-seated landslides in bedrock can relate to increased precipitation and groundwater recharge (Guglielmi et al., 2005; Vallet et al., 2016; Lacroix et al., 2020). At the Mannen instability, a part of the unstable slope failed in September 2019 (Kristensen et al., in review), possibly following changes in permafrost or deep seasonal frost. However, during several previous years, this rock mass reacted with increased sensitivity to precipitation, specifically at the end of the warm summer season and in the autumn. Several documented Holocene rock-slope failures at Mannen relate to a climate deterioration with strongly increasing precipitation around 5 ka (Hilger et al., 2018), which supports the slopes' sensitivity to high precipitation and snowmelt.

Exogenic drivers connected to snow melt and precipitation may also be relevant for the Skjeringahaugane instability, where deep post-glacial permafrost penetration was unlikely owing to its low elevation and late deglaciation, leaving the slope sensitive to such climatic changes. Here, the activation of the third and youngest sliding surface sampled in profile 3 (Fig. 2b) falls into a period where temperatures are high and precipitation rates are increasing after a period of lower rates (Fig. 10). The geodetically measured vertical deformation rates of ~0.3 cm a^{-1} are higher than the paleo-slip rates of 0.15 cm a^{-1} of the last 1.3 ka but are very similar to the average deformation rate of 0.33 cm a^{-1} (Table 4).

6. Conclusions

From this study the following conclusions can be drawn:

- Age constraints along vertical transects of seven sliding surfaces produced by active rock-slope instabilities in Norway resulted in logical chronological sequences, indicating gradual deformation along the sliding surfaces.
- Holocene slip rates have generally decreased over time. Recently measured deformation suggests a significant increase in sliding rates for Mannen and Gamanjunni 3, and a moderate acceleration for the upper area of Skjeringahaugane and Revdalsfjellet 2, both in western and northern Norway.
- Two of eight studied sliding surfaces seemed to have been activated during or shortly after local deglaciation at 16-14 and 11-10 ka, respectively, and were probably triggered by debuttressing effects, in addition to long term rock fatigue. Initial deformation at the Mannen and Revdalsfjellet 2 rockslides coincides with the peak of the HTM around 8 ka, reacting faster than the Gamanjunni 3 rockslide to increased temperatures and probably permafrost degradation. Estimated activation timing of the three remaining rockslides are spread from 5.6 to 4.4 ka, at the end of the HTM.
- Recently accelerating slip rates at Mannen, Revdalsfjellet and Gamanjunni seem to be attributed to atmospheric warming since the LIA and connected to permafrost degradation. Moderate acceleration in the upper part of the low elevation site Skjeringahaugane may be driven by increased precipitation

rates and intensities because this rock-slope instability has likely never been affected by deep permafrost penetration.
- Degrading permafrost might play a significant role in slope destabilisation in Norway. Mannen in southern Norway and Revdalsfjellet and Gamanjunni 3 in northern Norway are very likely to have experienced permafrost fluctuations throughout the Holocene, where permafrost dynamics and degradation is likely a first order control on past and modern slope activities.

Note on author contributions

The first author **PH** wrote the manuscript and carried out parts of the field work, processing, and analyses of the new data. She also developed the presented approach for calculating shielding on steep rock walls and analysed and re-/calculated previously published exposure ages. **RLH** contributed significantly with the project idea, sampling strategy, most of the field work and by providing pre-existing data. **JCG** supervised the sample processing, carried out the data reduction and supported PH during sample processing, analysis and age calculations. **KSM** developed the CryoGrid2D, together with Dr. S. Westermann, Department of Geosciences, UiO. KSM did initial runs from the study sites. **JC** further developed the code and boundary conditions, and made the runs presented in this study. **BE** was the leader of the RCN-funded CryoWALL project (243784/CLE) and contributed to the concept of thermal influence on the long-term stability of steep slope in the study areas. All authors contributed to the writing and revision of the paper.

Funding

This study is part of the project 'CryoWALL – Permafrost slopes in Norway' [grant number CLE/243784] funded by the Research Council of Norway (RCN). Additional funding was provided by the Geological Survey of Norway, Trondheim, and the Department of Geosciences, Univeristy of Oslo, Norway. JCG acknowledges support for the TCN laboratory from Canada Foundation for Innovation [grant numbers NSERC/21305 and NSRIT/36158].

Declaration of competing interest

The authors declare that they have no known competing financial interests or personal relationships that could have appeared to influence the work reported in this paper.

Acknowledgements

The ^{10}Be and ^{36}Cl sample preparation was mostly completed by G. Yang and partly by the first author at CRISDal Lab at Dalhousie University. Field assistance was provided by T. Redfield (NGU), B. Altena, F. Magnin and Ingvild Solheim (all UiO). Thanks also to S. Marrero for valuable support dealing with the correction for inherited ^{36}Cl concentrations at the Mannen study site. Finally, we thank two anonymous reviewers for their valuable comments, which helped improving the manuscript.

Appendix A. Supplementary data

Supplementary data to this article can be found online at https://doi.org/10.1016/j.quascirev.2020.106718.

References

Agliardi, A., Riva, F., Barbarano, M., Zanchetta, S., Scotti, R., Zanchi, A., 2019. Effects of tectonic structures and long-term seismicity on paraglacial giant slope deformations: piz Dora (Switzerland). Eng. Geol. 263 https://doi.org/10.1016/j.enggeo.2019.105353.

Agliardi, F., Scuderi, M.M., Fusi, N., Collettini, C., 2020. Slow-to-fast transition of giant creeping rockslides modulated by undrained loading in basal shear zones. Nat. Commun. 11 (1352) https://doi.org/10.1038/s41467-020-15093-3.

Amitrano, D., Helmstetter, A., 2006. Brittle creep, damage, and time to failure in rocks. J. Geophys. Res.: Solid Earth 111. https://doi.org/10.1029/2005JB004252.

Andersen, J.L., Egholm, D.L., Knudsen, M.F., Linge, H., Jansen, J.D., Pedersen, V.K., Nielsen, S.B., Tikhomirov, D., Olsen, J., Fabel, D., Xu, S., 2018. Widespread erosion on high plateaus during recent glaciations in Scandinavia. Nat. Commun. 9 (830) https://doi.org/10.1038/s41467-018-03280-2.

Balco, G., 2014. Simple computer code for estimating cosmic-ray shielding by oddly shaped objects. Quat. Geochronol. 11, 175–182. https://doi.org/10.1016/j.quageo.2013.12.002.

Ballantyne, C.K., 2002. A general model of paraglacial landscape response. Holocene 12, 371–376. https://doi.org/10.1191/0959683602hl553fa.

Ballantyne, C.K., Sandemann, G.F., Stone, J.O., Wilson, P., 2014. Rock-slope failure following Late Pleistocene deglaciation on tectonically stable mountainous terrain. Quat. Sci. Rev. 86, 144–157. https://doi.org/10.1016/j.quascirev.2013.12.021.

Ballantyne, C.K., Stone, J.O., Fifield, L.K., 1998. Cosmogenic Cl-36 dating of postglacial landsliding at the Storr, Isle of Skye, Scotland. Holocene 8, 347–351. https://doi.org/10.1191/095968398666797200.

Baroň, I., Sokol, L., Melichar, R., Plan, L., 2019. Gravitational and tectonic stress states within a deep-seated gravitational slope deformation near the seismogenic Periadriatic Line fault. Eng. Geol. 261, 105284. https://doi.org/10.1016/j.enggeo.2019.105284.

Bellwald, B., Hjelstuen, B.O., Sejrup, H.P., Stokowy, T., Kuvås, J., 2019. Holocene mass movements in west and mid-Norwegian fjords and lakes. Mar. Geol. 407, 192–212. https://doi.org/10.1016/j.margeo.2018.11.007.

Bhasin, R., Kaynia, A.M., 2004. Static and dynamic simulation of a 700-m high rock slope in western Norway. Eng. Geol. 71 (3–4), 213–226. https://doi.org/10.1016/S0013-7952(03)00135-2.

Bigot-Cormier, F., Braucher, R., Bourles, D., Guglielmi, Y., Dubar, M., Stephan, J., 2005. Chronological constraints on processes leading to large active landslides. Earth Planet Sci. Lett. 235, 141–150. https://doi.org/10.1016/j.epsl.2005.03.012.

Blikra, L.H., Braathen, A., Anda, E., Stalsberg, K., Longva, O., 2002. Rock Avalanches, Gravitational Bedrock Fractures and Neotectonic Faults Onshore Northern West Norway: Examples, Regional Distribution and Triggering Mechanisms. (NGU Report No. 2002.016). Norges geologiske undersøkelse, Trondheim.

Blikra, L.H., Christiansen, H.H., 2014. A field-based model of permafrost-controlled rockslide deformation in northern Norway. Geomorphology 208, 34–49. https://doi.org/10.1016/j.geomorph.2013.11.014.

Blikra, L.H., Fasani, G.B., Esposito, C., Lenti, L., Martino, S., Pecci, M., Mugnozza, G.S., Kalenchuk, K.S., Hutchinson, D.J., Diederichs, M., et al., 2012. The Aknes rockslide, Norway. In: Clague, J., Stead, D. (Eds.), Landslides: Types, Mechanisms and Modeling. Cambridge University Press, pp. 323–335. https://doi.org/10.1017/CBO9780511740367.

Blikra, L.H., Majala, G., Anda, E., Berg, H., Eikenæs, O., Helgås, G., Oppikofer, T., Hermanns, R.L., Böhme, M., 2016. Fare- Og Risikoklassifisering Av Ustabile Fjellparti - Faresoner, Arealhåndtering Og Tiltak (NVE No. 77–2016).

Blikra, L.H., Nemec, W., 1998. Postglacial colluvium in western Norway: depositional processes, facies and palaeoclimatic record. Sedimentology 45 (5), 909–959. https://doi.org/10.1046/j.1365-3091.1998.00200.x.

Böhme, M., Bunkholt, H., Dehls, J., Oppikofer, T., Hermanns, R.L., Dalsegg, E., Kristensen, L., Lauknes, T.R., Eriksen, H.Ø., 2016a. Geologisk Modell Og Fare- Og Risikoklassifisering Av Det Ustabile Fjellpartiet Gamanjunni 3 I Manndalen, Troms (NGU Report No. 2016.031). Norges geologiske undersøkelse, Trondheim.

Böhme, M., Bunkholt, H.S.S., Oppikofer, T., Dehls, J.F., Hermanns, R.L., Eriksen, H.Ø., Lauknes, T.R., Eiken, T., 2016b. Using 2D InSAR, dGNSS and structural field data to understand the deformation mechanism of the unstable rock slope Gamanjunni 3, northern Norway. In: Aversa, S., Cascini, L., Picarelli, L., Scavi, C. (Eds.), Landslides and Engineered Slopes. Experience, Theory and Practice. Proceedings of the 12th International Symposium on Landslides (Napoli, Italy, 12-19 June 2016). CRC Press, p. 443. https://doi.org/10.1201/9781315375007-35.

Böhme, M., Hermanns, R.L., Gosse, J., Hilger, P., Eiken, T., Lauknes, T.R., Dehls, J.F., 2019. Comparison of monitoring data with paleo–slip rates: cosmogenic nuclide dating detects acceleration of a rockslide. Geology 47 (4), 339–342. https://doi.org/10.1130/G45684.1.

Böhme, M., Hermanns, R.L., Oppikofer, T., Fischer, L., Bunkholt, H.S.S., Eiken, T., Pedrazzini, A., Derron, M.-H., Jaboyedoff, M., Blikra, L.H., Nilsen, B., 2013. Analyzing complex rock slope deformation at Stampa, western Norway, by integrating geomorphology, kinematics and numerical. Eng. Geol. 154, 116–130. https://doi.org/10.1016/j.enggeo.2012.11.016.

Böhme, M., Oppikofer, T., Longva, O., Jaboyedoff, M., Hermanns, R.L., Derron, M.-H., 2015b. Analyses of past and present rock slope instabilities in a fjord valley: implications for hazard estimations. Geomorphology 248, 464–474. https://doi.org/10.1016/j.geomorph.2015.06.045.

Booth, A.M., Dehls, J., Eiken, T., Fischer, L., Hermanns, R.L., Oppikofer, T., 2015. Integrating diverse geologic and geodetic observations to determine failure mechanisms and deformation rates across a large bedrock. Landslides 12 (4), 745–756. https://doi.org/10.1007/s10346-014-0504-y.

Braathen, A., Blikra, L.H., Berg, S.S., Karlsen, F., 2004. Rock-slope failures of Norway, type, geometry deformation mechanisms and stability. Nor. Geol. Tidsskr. 84, 67–88.

Březný, M., Pánek, T., Lenart, J., Zondervan, A., Braucher, R., 2018. ^{10}Be dating reveals pronounced Mid-to Late Holocene activity of deep-seated landslides in the highest part of the Czech Flysch Carpathians. Quat. Sci. Rev. 195, 180–194. https://doi.org/10.1016/j.quascirev.2018.07.030.

Brideau, M.-A., Yan, M., Stead, D., 2009. The role of tectonic damage and brittle rock fracture in the development of large rock slope failures. Geomorphology 103 (1), 30–49. https://doi.org/10.1016/j.geomorph.2008.04.010.

Brückl, E.P., 2001. Cause-effect models of large landslides. Nat. Hazards 23 (2–3), 291–314. https://doi.org/10.1023/A:1011160810423.

Caseldine, C., Langdon, P., Holmes, N., 2006. Early Holocene climate variability and the timing and extent of the Holocene termal maximum (HTM) in northern Iceland. Quat. Sci. Rev. 25, 2314–2331. https://doi.org/10.1016/j.quascirev.2006.02.003.

Chmeleff, J., von Blanckenburg, F., Kossert, K., Jakob, D., 2010. Determination of the ^{10}Be half-life by multicollector ICP-MS and liquid scintillation counting. Nucl. Instrum. Methods Phys. Res. Sect. B Beam Interact. Mater. Atoms 268 (2), 192–199 https://doi.org./10.1016/j.nimb.2009.09.012.

Clark, P.U., Dyke, A.S., Shakun, J.D., Carlson, A.E., Clark, J., Wohlfarth, B., Mitrovica, J.X., Hostetler, S.W., McCabe, A.M., 2009. The last glacial maximum. Science 325, 710–714. https://doi.org/10.1126/science.1172873.

Clauser, C., Huenges, E., 1995. Thermal conductivity of rocks and minerals. In: Ahrens, T.J. (Ed.), Rock Physics & Phase Relations. https://doi.org/10.1029/RF003p0105.

Cornelius, R.R., Scott, P.A., 1993. A materials failure relation of accelerating creep as empirical description of damage accumulation. Rock Mech. Rock Eng. 26, 233–252. https://doi.org/10.1007/BF01040117.

Crosta, G.B., Agliardi, F., 2003. Failure forecast for large rock slides by surface displacement measurements. Can. Geotech. J. 40, 176–191. https://doi.org/10.1139/t02-085.

Crozier, M.J., 2010. Deciphering the effect of climate change on landslide activity: a review. Geomorphology 124, 260–267. https://doi.org/10.1016/j.geomorph.2010.04.009.

Crozier, M.J., Glade, T., 2005. Landslide Hazard and Risk: Issues, Concepts and Approach. Wiley Chichester, pp. 1–40. https://doi.org/10.1002/9780470012659.ch1 chap. 1.

Cruden, D.M., 1971. The form of the creep law for rock under uniaxial compression. Int. J. Rock Mech. Min. Sci. Geomech. Abstr. 8, 105–126. https://doi.org/10.1016/0148-9062(71)90003-9.

Dabrowski, M., Krotkiewski, M., Schmid, D.W., 2008. MILAMIN: MATLAB-based finite element method solver for large problems. Geochem. Geophys. Geosystems 9. https://doi.org/10.1029/2007GC001719.

Dahle, H., Anda, E., Saintot, A., Sætre, S., 2008. Faren for fjellskred fra fjellet Mannen i Romsdalen (NGU Rapport No. 2008.087). Norges Geologiske Undersøkelse, Trondheim.

Derron, M.-H., Jaboyedoff, M., Blikra, L.H., 2005. Preliminary assessment of rockslide and rockfall hazards using a DEM (Oppstadhornet, Norway). Nat. Hazards Earth Syst. Sci. 5, 285–292. https://doi.org/10.5194/nhess-5-285-2005.

Dortch, J.M., Owen, L.A., Haneberg, W.C., Caffee, M.W., Dietsch, C., Kamp, U., 2009. Nature and timing of large landslides in the Himalaya and Transhimalaya of northern India. Quat. Sci. Rev. 28 (11–12), 1037–1054. https://doi.org/10.1016/j.quascirev.2008.05.002.

Dyrrdal, A.V., Isaksen, K., Hygen, H.O., Meyer, N.K., 2012. Changes in meteorological variables that can trigger natural hazards in Norway. Clim. Res. 55, 153–165. https://doi.org/10.3354/cr01125.

Eberhardt, E., Kaiser, P.K., Stead, D., 2002. Numerical analysis of progressive failure in natural rock slopes. In: Presented at the EUROCK 2002 - ISRM International Symposium on Rock Engineering for Mountainous Regions. Funchal, Madeira, pp. 145–153.

Eberhardt, E., Stead, D., Coggan, J.S., 2004. Numerical analysis of initiation and progressive failure in natural rock slopes - the 1991 Randa rockslide. Int. J. Rock Mech. Min. Sci. 41, 69–87. https://doi.org/10.1016/S1365-1609(03)00076-5.

Eisbacher, G.H., Clague, J.J., 1984. Destructive mass movements in high mountains: hazard and management. Geol. Survey Canada vols. 84–16, 230.

Evans, S.G., Clague, J.J., 1994. Recent climatic change and catastrophic geomorphic processes in mountain environments. Geomorphology 10 (1), 107–128. https://doi.org/10.1016/0169-555X(94)90011-6.

Furseth, A., 1985. Dommedagsfjellet - Tafjord 1934. Gyldendal Norsk Forlag A/S.

Gischig, V., Preisig, G., Eberhardt, E., 2016. Numerical investigation of Seismically induced rock mass fatigue as a mechanism contributing to the progressive failure of deep-seated landslides. Rock Mech. Rock Eng. 49, 2457–2478. https://doi.org/10.1007/s00603-015-0821-z.

Gisnås, K., Etzelmüller, B., Farbrot, H., Schuler, T.V., Westermann, S., 2013. CryoGRID 1.0: permafrost distribution in Norway estimated by a spatial numerical model: CryoGRID 1.0: permafrost distribution in Norway. Permafr. Periglac. Process. 24, 2–19. https://doi.org/10.1002/ppp.1765.

Gisnås, K., Etzelmüller, B., Lussana, C., Hjort, J., Sannel, A.B.K., Isaksen, K., Westermann, S., Kuhry, P., Christiansen, H.H., Frampton, A., Åkerman, J., 2017. Permafrost map for Norway, Sweden and Finland. Permafr. Periglac. Process. 28, 359–378. https://doi.org/10.1002/ppp.1922.

Gosse, J.C., Phillips, F., 2001. Terrestrial in situ cosmogenic nuclides: theory and application. Quat. Sci. Rev. 20, 1475–1560. https://doi.org/10.1016/S0277-3791(00)00171-2.

Grämiger, L.M., Moore, J.R., Gischig, V.S., Ivy-Ochs, S., Loew, S., 2017. Beyond debuttressing: mechanics of paraglacial rock slope damage during repeat glacial cycles. J. Geophys. Res.: Earth Surf. 122 (4), 1004–1036. https://doi.org/10.1002/2016JF003967.

Grimstad, E., Nesdal, S., 1991. Loen Rockslides. A Historical Review. Norwegian Geotechnical Institute (NGI).

Gruber, S., Haeberli, W., 2007. Permafrost in steep bedrock slopes and its temperature-related destabilization following climate change. J. Geophys. Res.: Earth Surf. 112 https://doi.org/10.1029/2006JF000547.

Guglielmi, Y., Cappa, F., Binet, S., 2005. Coupling between hydrogeology and deformation of mountainous rock slopes: insights from La Clapière area (southern Alps, France). Compt. Rendus Geosci. 337 (13), 1154–1163. https://doi.org/10.1016/j.crte.2005.04.016.

Gunzburger, Y., Merrien-Soukatchoff, V., Guglielmi, Y., 2005. Landslide Influence of daily surface temperature fluctuations on rock slope stability: case study of the Rochers de Valabres slope (France). Int. J. Rock Mech. Min. Sci. 42, 331–349. https://doi.org/10.1016/j.ijrmms.2004.11.003.

Guzzetti, F., 2000. Landslide fatalities and the evaluation of landslide risk in Italy. Eng. Geol. 58, 89–107. https://doi.org/10.1016/S0013-7952(00)00047-8.

Haefeli, R., 1953. Creep problems in soils, snow and ice. In: Proceedings of the 3rd International Conference on Soil Mechanics and Foundation Engineering, Zurich, Versuchsanst. F. Wasserbau U. Erdbau Eidgenoess. Tech. Hochschule, Zuerich, Switzerland, vol. 3, pp. 238–251.

Hales, T.C., Roering, J.J., 2007. Climatic controls on frost cracking and implications for the evolution of bedrock landscapes. J. Geophys. Res. 112, F02033. https://doi.org/10.1029/2006JF000616.

Hall, A.M., Ebert, K., Kleman, J., Nesje, A., Ottesen, D., 2013. Selective glacial erosion on the Norwegian passive margin. Geology 41, 1203–1206. https://doi.org/10.1130/G34806.1.

Hancox, G.T., McSaveney, M.J., Manville, V.R., Davies, T.R., 2005. The October 1999 Mt Adams rock avalanche and subsequent landslide dam-break flood and effects in Poerua river, Westland, New Zealand. N. Z. J. Geol. Geophys. 48, 683–705. https://doi.org/10.1080/00288306.2005.9515141.

Hermanns, Reginald L., Niedermann, Samuel, Ivy-Ochs, Susan, Kubik, Peter W., 2004. Rock avalanching into a landslide-dammed lake causing multiple dam failure in Las Conchas valley (NW Argentina)? Evidence from surface exposure dating and stratigraphic analyses. Landslides 1 (2), 113–122. https://doi.org/10.1007/s10346-004-0013-5.

Hermanns, R., Niedermann, S., Villanueva Garcia, A., Schellenberger, A., 2006. Rock avalanching in the NW Argentine Andes as a result of complex interactions of lithologic, structural and topographic boundary conditions, climate change and active tectonics: landslides from massive rock slope failure. NATO Sci. Ser. IV 49, 539–569.

Hermanns, R.L., Fischer, L., Oppikofer, T., Böhme, M., Dehls, J.F., Henriksen, H., Booth, A., Eilertsen, R., Longva, O., Eiken, T., 2011. Mapping of Unstable and Potentially Unstable Rock Slopes in Sogn Og Fjordane (Work Report 2008-2010) (NGU Rapport No. 2011.055). Norges Geologiske Undersøkelse, Trondheim.

Hermanns, R.L., Oppikofer, T., Anda, E., Blikra, L.H., Böhme, M., Bunkholt, H., Crosta, G., Dahle, H., Devoli, G., Fischer, L., others, 2013a. Hazard and risk classification for large unstable rock slopes in Norway. In: International Conference Vajont 1963-2013. Thoughts and Analyses after 50 Years since the Catastrophic Landslide, Padua, Italy – 8-10 October 2013. Italian Journal of Engineering Geology and Environment - Book Series (6). Sapienza Università Editrice, pp. 245–254.

Hermanns, R.L., Oppikofer, T., Dahle, H., Eiken, T., Ivy-Ochs, S., Blikra, L.H., 2013b. Understanding long-term slope deformation for stability assessment of rock slopes: the case of the Oppstadhornet rockslide, Norway. In: International Conference Vajont 1963-2013. Thoughts and Analyses after 50 Years since the Catastrophic Landslide, Padua, Italy – 8-10 October 2013. Italian Journal of Engineering Geology and Environment - Book Series (6). Sapienza Università Editrice, pp. 255–264.

Hermanns, R.L., Redfield, T.F., Bunkholt, H.S.S., Fischer, L., Oppikofer, T., 2012. Cosmogenic nuclide dating of slow moving rockslides in Norway in order to assess long-term slide velocities. In: Eberhardt, E.B., Froese, C., Turner, A.K., Leroueil, S. (Eds.), Landslides and Engineered Slopes: Protecting Society through Improved Understanding : Proceedings of the 11th International and 2nd North American Symposium on Landslides and Engineered Slopes, Banff, Canada, 3-8 June 2012. Taylor & Francis, London, pp. 849–854.

Hermanns, R.L., Schleier, M., Böhme, M., Blikra, L.H., Gosse, J., Ivy-Ochs, S., Hilger, P., 2017. Rock-avalanche activity in W and S Norway peaks after the retreat of the Scandinavian ice sheet. In: Mikoš, M., Vilímek, V., Yin, Y., Sassa, K. (Eds.), Advancing Culture of Living with Landslides. Springer International Publishing, Cham, pp. 331–338. https://doi.org/10.1007/978-3-319-53483-1_39.

Hermanns, R.L., Strecker, M.R., 1999. Structural and lithological controls on large Quaternary rock avalanches (sturzstroms) in arid northwestern Argentina. Geol. Soc. Am. Bull. 111 (6), 934–948. https://doi.org/10.1130/0016-7606(1999)111<0934:SALCOL>2.3.CO;2.

Hilger, P., Gosse, J.C., Hermanns, R.L., 2019. How significant is inheritance when dating rockslide boulders with terrestrial cosmogenic nuclide dating?—a case study of an historic event. Landslides 16, 729–738. https://doi.org/10.1007/s10346-018-01132-0.

Hilger, P., Hermanns, R.L., Gosse, J.C., Jacobs, B., Etzelmüller, B., Krautblatter, M., 2018. Multiple rock-slope failures from Mannen in Romsdal Valley, western Norway, revealed from Quaternary geological mapping and 10Be exposure dating. The Holocene. https://doi.org/10.1177/0959683618798165.

Huggel, C., Allen, S., Deline, P., Fischer, L., Noetzli, J., Ravanel, L., 2012. Ice thawing, mountains falling - are alpine rock slope failures increasing? Geol. Today 28 (3), 98–104. https://doi.org/10.1111/j.1365-2451.2012.00836.x.

Hughes, A.L.C., Gyllencreutz, R., Lohne, Ø.S., Mangerud, J., Svendsen, J.I., 2016. The last Eurasian ice sheets - a chronological database and time-slice reconstruction, DATED-1. Boreas 45, 1–45. https://doi.org/10.1111/bor.12142.

Hutchinson, J.N., 1988. General Report: Morphological and Geotechnical Parameters of Landslides in Relation to Geology and Hydrogeology: Proc 5th International Symposium on Landslides, Lausanne, 10–15 July 1988V1. https://doi.org/10.1016/0148-9062(89)90310-0. P3–35. Publ. Rotterdam: A.A. Balkema 3–35.

Ivy-Ochs, S., Poschinger, A.v., Synal, H.-A., Maisch, M., 2009. Surface exposure dating of the Flims landslide, Graubünden, Switzerland. Geomorphology 103, 104–112. https://doi.org/10.1016/j.geomorph.2007.10.024.

Jaboyedoff, M., Derron, M.H., 2005. Hazard assessment within an integrated risk assessment process for landslides (IRAPL). In: Proceedings of the International Conference on Landslide Risk Management (Vancouver, Balkema).

Jia, H., Xiang, W., Krautblatter, M., 2015. Quantifying rock fatigue and decreasing compressive and tensile strength after repeated freeze-thaw cycles. Permafr. Periglac. Process. 26, 368–377. https://doi.org/10.1002/ppp.1857.

Johnsen, S.J., Dahl-Jensen, D., Dansgaard, W., Gundestrup, N., 1995. Greenland palaeotemperatures derived from GRIP bore hole temperature and ice core isotope profiles. Tellus B: Chem. Phys. Meteorol. 47 (5), 624–629. https://doi.org/10.1034/j.1600-0889.47.issue5.9.x.

Keuschnig, M., Hartmeyer, I., Höfer-Öllinger, G., Schober, A., Krautblatter, M., Schrott, L., 2015. Permafrost-related mass movements: implications from a rock slide at the Kitzsteinhorn, Austria. In: Lollino, G., Manconi, A., Clague, J., Shan, W., Chiarle, M. (Eds.), Engineering Geology for Society and Territory - Volume 1. Springer, Cham. https://doi.org/10.1007/978-3-319-09300-0_48.

Kleman, J., 1994. Preservation of landforms under ice sheets and ice caps. Geomorphology 9, 19–32. https://doi.org/10.1016/0169-555X(94)90028-0.

Korschinek, G., Bergmaier, A., Faestermann, T., Gerstmann, U.C., Knie, K., Rugel, G., Wallner, A., Dillmann, I., Dollinger, G., von Gostomski, C.L., Kossert, K., Maiti, M., Poutivtsev, M., Remmert, A., 2010. A new value for the half-life of ^{10}Be by Heavy-Ion Elastic Recoil Detection and liquid scintillation counting. Nucl. Instrum. Methods Phys. Res. Sect. B Beam Interact. Mater. Atoms 268, 187–191. https://doi.org/10.1016/j.nimb.2009.09.020.

Krautblatter, M., Funk, D., Günzel, F.K., 2013. Why permafrost rocks become unstable: a rock-ice-mechanical model in time and space: a rock-ice-mechanical model for permafrost rocks. Earth Surf. Process. Landforms 38, 876–887. https://doi.org/10.1002/esp.3374.

Kristensen, L., Czekirda, J., Penna, I., Etzelmüller, B., Nicolet, P., Pullarello, J.S., Blikra, L.H., Abellan, A., Skrede, I., Oldani, S., 2020. Movements, Failure and Climatic Control of the Veslemannen Rockslide. Western Norway (Landslides, in review).

Lacroix, P., Amitrano, D., 2013. Long-term dynamics of rockslides and damage propagation inferred from mechanical modeling: long-term dynamics of rockslides. J. Geophys. Res.: Earth Surf. 118, 2292–2307. https://doi.org/10.1002/2013JF002766.

Lacroix, P., Handwerger, A.L., Bièvre, G., 2020. Life and death of slow-moving landslides. Nat. Rev. Earth Environ. 1, 404–419. https://doi.org/10.1038/s43017-020-0072-8.

Le Roux, O., Schwartz, S., Gamond, J.F., Jongmans, D., Bourles, D., Braucher, R., Mahaney, W., Carcaillet, J., Leanni, L., 2009. CRE dating on the head scarp of a major landslide (Séchilienne, French Alps), age constraints on Holocene kinematics. Earth Planet Sci. Lett. 280, 236–245. https://doi.org/10.1016/j.epsl.2009.01.034.

Lebrouc, V., Schwartz, S., Baillet, L., Jongmans, D., Gamond, J.F., 2013. Modeling permafrost extension in a rock slope since the Last Glacial Maximum: application to the large Sèchilienne landslide (French Alps). Geomorphology 198, 189–200. https://doi.org/10.1016/j.geomorph.2013.06.001.

Lifton, N., 2016. Implications of two Holocene time-dependent geomagnetic models for cosmogenic nuclide production rate scaling. Earth Planet Sci. Lett. 433, 257–268. https://doi.org/10.1016/j.epsl.2015.11.006.

Lilleøren, K.S., Etzelmüller, B., Schuler, T.V., Gisnås, K., Humlum, O., 2012. The relative age of mountain permafrost — estimation of Holocene permafrost limits in Norway. Global Planet. Change 92 (93), 209–223. https://doi.org/10.1016/j.gloplacha.2012.05.016.

Liu, Z., Otto-Bliesner, B.L., He, F., Brady, E.C., Tomas, R., Clark, P.U., Carlson, A.E., Lynch-Stieglitz, J., Curry, W., Brook, E., Erickson, D., Jacob, R., Kutzbach, J., Cheng, J., 2009. Transient simulation of last deglaciation with a new mechanism for Bølling-Allerød warming. Science 325, 310–314. https://doi.org/10.1126/science.1171041.

Lund, B., Näslund, J., 2009. Glacial isostatic adjustment: implications for glacially induced faulting and nuclear waste repositories. In: Connor, C., Chapman, N., Connor, L. (Eds.), Volcanic and Tectonic Hazard Assessment for Nuclear Facilities. Cambridge University Press, Cambridge, pp. 142–155. https://10.1017/CBO9780511635380.006.

Magnin, F., Etzelmüller, B., Westermann, S., Isaksen, K., Hilger, P., Hermanns, R.L., 2019. Permafrost distribution in steep rock slopes in Norway: measurements, statistical modelling and implications for geomorphological processes. Earth Surface Dynam. 7 (4), 1019–1040. https://doi.org/10.5194/esurf-7-1019-2019.

Mamot, P., Weber, S., Schröder, T., Krautblatter, M., 2018. A temperature-and stress-controlled failure criterion for ice-filled permafrost rock joints. The Chryosphere 12, 3333–3353. https://doi.org/10.5194/tc-12-3333-2018.

Marrero, S.M., Phillips, F.M., Borchers, B., Lifton, N., Aumer, R., Balco, G., 2016a. Cosmogenic nuclide systematics and the CRONUScalc program. Quat. Geochronol. 31, 160–187. https://doi.org/10.1016/j.quageo.2015.09.005.

Marrero, S.M., Phillips, F.M., Caffee, M.W., Gosse, J.C., 2016b. CRONUS-Earth cosmogenic 36Cl calibration. Quat. Geochronol. 31, 199–219. https://doi.org/10.1016/j.quageo.2015.10.002.

Mauri, A., Davis, B.A.S., Collins, P.M., Kaplan, J.O., 2015. The climate of Europe during the Holocene: a gridded pollen-based reconstruction and its multi-proxy evaluation. Quat. Sci. Rev. 112, 109–127. https://doi.org/10.1016/j.quascirev.2015.01.013.

McColl, S.T., 2012. Paraglacial rock-slope stability. Geomorphology 153–154, 1–16. https://doi.org/10.1016/j.geomorph.2012.02.015.

Moore, J.R., Gischig, V., Katterbach, M., Loew, S., 2011. Air circulation in deep fractures and the temperature field of an alpine rock slope. Earth Surf. Process. Landforms 36 (15), 1985–1996. https://doi.org/10.1002/esp.2217.

Murton, J.B., Peterson, R., Ozouf, J.-C., 2006. Bedrock fracture by ice segregation in cold regions. Science 314 (5802), 1127–1129. https://doi.org/10.1126/science.1132127.

Myhra, K.S., 2016. Modelling Permafrost Conditions in Steep Mountain Environments (PhD Thesis). Univeristy of Oslo.

Myhra, K.S., Westermann, S., Etzelmüller, B., 2017. Modelled distribution and temporal evolution of permafrost in steep rock walls along a latitudinal transect in Norway by CryoGrid 2D. Permafr. Periglac. Process. 28, 172–182. https://doi.org/10.1002/ppp.1884.

NGU, 2020a. Ustabile Fjellparti. Nasjonal Database for Ustabile Fjellparti. https://geo.ngu.no/kart/ustabilefjellparti_mobil.

NGU, 2020b. Berggrunn. Nasjonal Berggrunnsdatabase. https://geo.ngu.no/kart/berggrunn_mobil.

North Greenland Ice Core Project Members (NGRIP), 2004. North Greenland Ice Core Project Oxygen Isotope Data. IGBP PAGES/World. Data Center for Paleoclimatology, Data Contribution Series # 2004-059. NOAA/NGDC Paleoclimatology Program, Boulder CO, USA.

NVE, 2017. Fjellskredovervaking - NVE. https://www.nve.no/flaum-og-skred/fjellskredovervaking/. (Accessed 30 October 2020).

Oppikofer, T., Nordahl, B., Bunkholt, H., Nicolaisen, M., Jarna, A., Iversen, S., Hermanns, R.L., Böhme, M., Yugsi Molina, F.X., 2015. Database and online map service on unstable rock slopes in Norway — from data perpetuation to public information. Geomorphology 249, 69–81. https://doi.org/10.1016/j.geomorph.2015.08.005.

Ostermann, M., Sanders, D., 2017. The Benner pass rock avalanche cluster suggests a close relation between long-term slope deformation (DSGSDs and translational rock slides) and catastrophic failure. Geomorphology 289, 44–59. https://doi.org/10.1016/j.geomorph.2016.12.018.

Pánek, T., 2015. Recent progress in landslide dating: a global overview. Prog. Phys. Geogr. 39, 168–198. https://doi.org/10.1177/0309133314550671.

Pánek, T., Mentlík, P., Engel, Z., Braucher, R., Zondervan, A., Aster Team, 2017. Late Quaternary sackungen in the highest mountains of the Carpathians. Quat. Sci. Rev. 159, 47–62. https://doi.org/10.1016/j.quascirev.2017.01.008.

Pareek, N., Sharma, M.L., Arora, M.K., 2010. Impact of seismic factors on landslide susceptibility zonation: a case study in part of Indian Himalayas. Landslides 7 (2), 191–201. https://doi.org/10.1007/s10346-009-0192-1.

Paterson, W.S.B., 1994. The Physics of Glaciers, Edition, vol. 3. Pergamon, p. 480.

Petley, D.N., Bulmer, M.H., Murphy, W., 2002. Patterns of movement in rotational and translational landslides. Geology 30 (8), 719–722. https://doi.org/10.1130/0091-7613(2002)030<0719:POMIRA>2.0.CO;2.

Pousse-Beltran, L., Vassallo, R., Audemard, F., Jouanne, F., Carcaillet, J., Pathier, E., Volat, M., 2017. Pleistocene slip rates on the Boconó fault along the north Andean block plate boundary, Venezuela: Pleistocene slip rates of the Boconó F. Tectonics 36, 1207–1231. https://doi.org/10.1002/2016TC004305.

Ravanel, L., Deline, P., 2011. Climate influence on rockfalls in high-Alpine steep rockwalls: the north side of the Aiguilles de Chamonix (Mont Blanc massif) since the end of the 'Little Ice Age. Holocene 21, 357–365. https://doi.org/10.1177/0959683610374887.

Renssen, H., Seppä, H., Heiri, O., Roche, D.M., Goosse, H., Fichefet, T., 2009. The spatial and temporal complexity of the Holocene thermal maximum. Nat. Geosci. 2 (6), 411–414. https://doi.org/10.1038/ngeo513.

Roberts, D., 2003. The Scandinavian Caledonides: event chronology, palaeogeographic settings and likely modern analogues. Tectonophysics 365, 283–299. https://doi.org/10.1016/S0040-1951(03)00026-X.

Roberts, N.J., Rabus, B.T., Clague, J.J., Hermanns, R.L., Guzmán, M.-A., Minaya, E., 2019. Changes in ground deformation prior to and following a large urban landslide in La Paz, Bolivia, revealed by advanced InSAR. Nat. Hazards Earth Syst. Sci. 19, 679–696. https://doi.org/10.5194/nhess-19-679-2019.

Saintot, A., Dahle, H., Derron, M.-H., Henderson, I., Oppikofer, T., 2012. Large gravitational rock slope deformation in Romsdalen valley (Western Norway). Rev. Asoc. Geol. Argent. 69 (3), 354–371.

Sanchez, G., Rolland, Y., Corsini, M., Braucher, R., Bourlès, D., Arnold, M., Aumaître, G., 2010. Relationships between tectonics, slope instability and climate change: cosmic ray exposure dating of active faults, landslides and glacial surfaces in the SW Alps. Geomorphology 117, 1–13. https://doi.org/10.1016/j.geomorph.2009.10.019.

Schleier, M., Hermanns, R.L., Krieger, I., Oppikofer, T., Eiken, T., Rønning, J.S., Rohn, J., 2016. Gravitational reactivation of a pre-existing post-Caledonian fault system: the deep-seated gravitational slope deformation at Middagstinden, western Norway. Norw. J. Geol. 96, 1–24. https://doi.org/10.17850/njg96-3-03.

Schleier, M., Hermanns, R.L., Rohn, J., Gosse, J.C., 2015. Diagnostic characteristics and paleodynamics of supraglacial rock avalanches, Innerdalen, Western Norway. Geomorphology 245, 23–39. https://doi.org/10.1016/j.geomorph.2015.04.033.

Shewchuk, J.R., 1996. Triangle: engineering a 2D quality mesh generator and

Delaunay triangulator. In: Lin, M.C., Manocha, D. (Eds.), Applied Computational Geometry towards Geometric Engineering. Springer Berlin Heidelberg, Berlin, Heidelberg, pp. 203–222. https://doi.org/10.1007/BFb0014497.
Slagstad, T., Balling, N., Elvebakk, H., Midttømme, K., Olesen, O., Olsen, L., Pascal, C., 2009. Component Parts of the World Heat Flow Data Collection. https://doi.org/10.1594/PANGAEA.805921. Pangaea.
Stead, D., Eberhardt, E., 2013. Understanding the mechanics of large landslides. Italian J. Eng. Geol. Environ. Book Ser. 6, 85–112. https://doi.org/10.4408/IJEGE.2013-06.B-07.
Steiger, C., Etzelmüller, B., Westermann, S., Myhra, K.S., 2016. Modelling the permafrost distribution in steep rock walls. Norw. J. Geol. 96 (4), 329–341. https://doi.org/10.17850/njg96-4-04.
Stroeven, A.P., Hättestrand, C., Kleman, J., Heyman, J., Fabel, D., Fredin, O., Goodfellow, B.W., Harbor, J.M., Jansen, J.D., Olsen, L., Caffee, M.W., Fink, D., Lundqvist, J., Rosqvist, G.C., Strömberg, B., Jansson, K.N., 2016. Deglaciation of fennoscandia. Quat. Sci. Rev. 147, 91–121. https://doi.org/10.1016/j.quascirev.2015.09.016.
Terzaghi, K., 1950. Mechanism of landslides. In: Paige, S. (Ed.), Application of Geology to Engineering Practice (Berkey). Geological Society of America, Washington D.C., pp. 83–123
Tesson, J., Benedetti, L., 2019. Seismic history from in situ 36Cl cosmogenic nuclide data on limestone fault scarps using Bayesian reversible jump Markov chain Monte Carlo. Quat. Geochronol. 52, 1–20. https://doi.org/10.1016/j.quageo.2019.02.004.
Tikhomirov, D., Akçar, N., Ivy-Ochs, S., Alfimov, V., Schlüchter, C., 2014. Calculation of shielding factors for production of cosmogenic nuclides in fault scarps. Quat. Geochronol. 19, 181–193. https://doi.org/10.1016/j.quageo.2013.08.004.
Tveten, E., Lutro, O., Thorsnes, T., 1998. Geologisk Kart over Norge, Berggrunnskart Ålesund, 1:250,000. Norges geologiske undersøkelse.
Vallet, A., Charlier, J.B., Fabbri, O., Bertrand, C., Carry, N., Mudry, J., 2016. Functioning and precipitation-displacement modelling of rainfall-induced deep-seated landslides subject to creep deformation. Landslides 13, 653–670. https://doi.org/10.1007/s10346-015-0592-3.
Weber, S., Beutel, J., Faillettaz, J., Hasler, A., Krautblatter, M., Vieli, A., 2017. Quantifying irreversible movement in steep, fractured bedrock permafrost on Matterhorn (CH). The Chryosphere 11 (1), 567–583. https://doi.org/10.5194/tc-11-567-2017.
Welkner, D., Eberhardt, E., Hermanns, R.L., 2010. Hazard investigation of the Portillo Rock Avalanche site, central Andes, Chile, using an integrated field mapping and numerical modelling approach. Eng. Geol. 114 (3–4), 278–297. https://doi.org/10.1016/j.enggeo.2010.05.007.
Xue, L., Qin, S., Li, P., Li, G., Oyediran, I.A., Pan, X., 2014. New quantitative displacement criteria for slope deformation process: from the onset of the accelerating creep to brittle rupture and final failure. Eng. Geol. 182, 79–87. https://doi.org/10.1016/j.enggeo.2013.08.007.
Yeager, S.G., Shields, C.A., Large, W.G., Hack, J.J., 2006. The low-resolution CCSM3. J. Clim. 19 (11), 2545–2566. https://doi.org/10.1175/JCLI3744.1.
Zerathe, S., Lebourg, T., Braucher, R., Bourlès, D., 2014. Mid-Holocene cluster of large-scale landslides revealed in the Southwestern Alps by 36Cl dating. Insight on an Alpine-scale landslide activity. Quat. Sci. Rev. 90, 106–127. https://doi.org/10.1016/j.quas.